Tuning the sorption ability of hydroxyapatite/carbon composites for the simultaneous remediation of wastewaters containing organic-inorganic pollutants

Michele Ferri[a, §], Sebastiano Campisi[a, §], Laura Polito[b], Jiany Shen[c], and Antonella Gervasini[a,*]

[a] Dipartimento di Chimica, Università degli Studi di Milano, Via Golgi 19, 20133 Milano, Italy

[b] CNR - Consiglio Nazionale delle Ricerche, SCITEC - Istituto di Scienze e Tecnologie Chimiche "Giulio Natta", Via G. Fantoli 16/15, 20138 Milano, Italy

[c] Laboratory of Mesoscopic Chemistry, School of Chemistry and Chemical Engineering, Nanjing University, 210023 Nanjing, China

* *Corresponding author*

§ *These authors contributed equally to the work*

ABSTRACT

In this paper, we report on the rational design, synthesis, characterization, and application of eco-friendly hydroxyapatite/carbon (HAP/C) composites as effective sorbents for the simultaneous remediation of organic-inorganic pollution in wastewaters. Carbon content in composites ranged from *ca*. 4 to *ca.* 20 wt.%. Structural and morphological features of the composites were studied by N_2 adsorption/desorption analyses, electron microscopy (TEM and HAADF-STEM/EDX) and X-ray powder diffraction (XRPD). These features were correlated with the composition and the exposure of surface functional groups. Surface acid-base groups were assessed by liquid-solid acid/base titrations and results depended on the composition ratio of the two components.

Batch adsorption tests, performed with various initial concentrations of pollutant species and dosages, proved that composites merged the sorption properties of the two moieties, being able to simultaneously adsorb organic (methylene blue) and inorganic (Cu(II) and Ni(II)) pollutants. On the optimal carbonaceous scaffold content (*ca*. 8 wt.% carbon), kinetic tests revealed that this composite could almost completely remove high concentrations of co-present pollutants, namely, Cu(II), Ni(II), (300 ppm) and methylene blue (250 ppm) in *ca*. 1 hour, with sorbent dosage of 10 g L^{-1}. In addition, leaching tests proved the permanent retention of the hazardous species on the composites.

KEYWORDS

Calcium phosphate, activated carbon, eco-friendly material, adsorption process, heavy metal pollution, organic dye

GRAPHICAL ABSTRACT

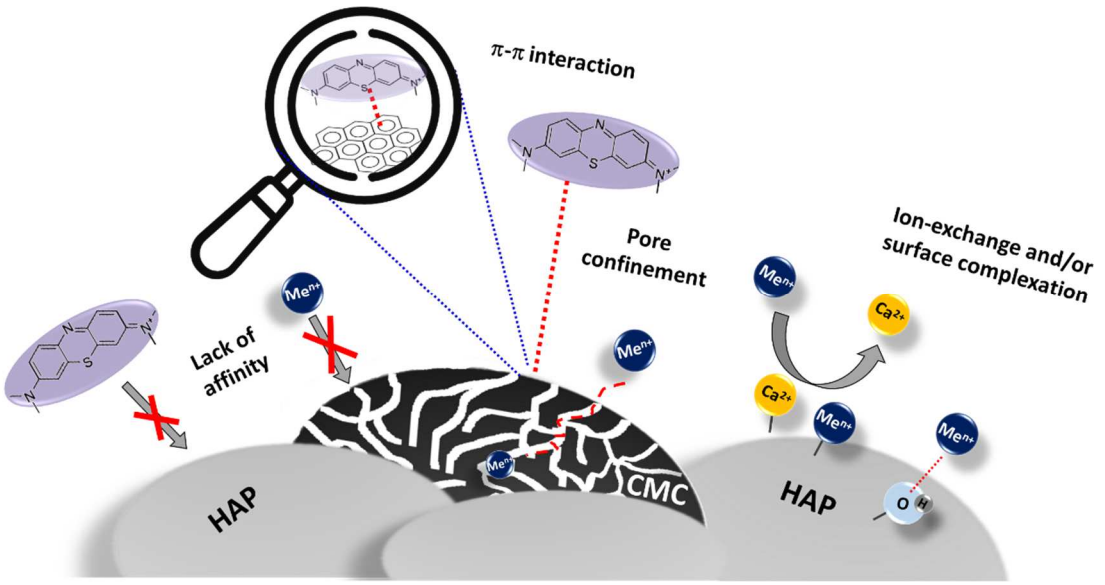

Graphical depiction of the interfacial phenomena of adsorption which take place at the solution-HAP/CMC composites interface, resulting in the simultaneous removal of organic and inorganic pollutants from wastewaters.

1. INTRODUCTION

Polluted waters from anthropogenic activities generally contain multiple pollutants [1] which belong to different classes of compounds [2]. Inorganic species (monoatomic anions as well as polyatomic species) account for *ca*. 30% of the pollutants detected in sewage waters [3]. Stringent legal limits are set for such species in both irrigation and drinking water because their chronic assumption is proven to cause bone degeneration, organ, blood, and soft tissue damage [4].

Organic species account for the remaining 70% of the pollutants [3]. In particular, with more than 3600 species currently under use in the textile sector and a discharge rate of *ca*. 20% in industrial effluents, dyes are potent heavy water pollutants [5]. These species exert long-lasting dangerous effects on aquatic organisms and exhibit proven carcinogenic and mutagenic effects on humans when ingested [6].

Wastewater remediation by adsorption is currently considered one of the most suitable options in terms of capital and operational costs, space occupation, operational flexibility and volume capability [3]. However, single sorbents are generally inadequate for the simultaneous remediation of organic-inorganic polluted streams [7]. Indeed, the major differences in physical and chemical properties of diverse pollutants call for materials with a dual nature, able to concurrently interact with both anions/cations and complex organic structures.

To tackle this issue, composite nano-scaled materials of different nature have been synthesized and tested in the remediation of polluted wastewater [8–10]. Nevertheless, the design of effective sorbents, which fulfill both cost and environmental requirements, remains a major challenge.

Hydroxyapatite (HAP, chemical formula $Ca_{10}(PO_4)_6(OH)_2$) is a mineral of the calcium phosphate family, considered an eco-friendly material in virtue of its non-toxicity, biocompatibility, and envisaged applications in environmental protection processes [11]. In addition to these features, it can be extracted from biowastes (mammalian bone, fishbone, eggshell, seashell, algae, plants and limestone) or chemically synthesized by several low-cost routes [12]. It possesses thermal and

chemical stability, structure flexibility, and marked water insolubility ($K_{ps} \approx 10^{-59}$ at 25°C) [13]. It has proven to be an effective sorbent for several inorganic hazardous species (e.g. F^- and heavy metal cations), which are retained by means of different mechanisms (ion-exchange, surface complexation and/or dissolution-precipitation, mainly depending on the sorbate) [11,14–19]. In addition, the immobilization of such species onto HAP surface is almost permanent [17,18]. By contrast, organic pollutants are hardly immobilized onto the hydrophilic HAP surface [20].

Carbonaceous materials (hereinafter generally referred to as C) and in particular activated carbons (AC) are the state-of-art sorbents for organic pollutants thanks to their large surface area and porosity, surface functionalization degree and ability to establish π–π interactions with complex aromatic molecules [4]. Eco-friendly production of activated carbons may be achieved employing biomass wastes and agricultural by-products as carbon sources [6,21]. While, functionalization and/or templating may be carried out using common reagents/templating agents such as HNO_3 and $ZnCl_2$, respectively [22,23]. Activated carbons exhibit modest affinity towards inorganic polluting agents in the form of ions, with consequent limited adsorption capacity and retention ability [4].

Based on HAP and C complementary features, the proper design of HAP/C composites may pave the way for the generation of effective sorbents, with their dual nature guaranteeing fast, effective and simultaneous removal of diverse polluting species from wastewater. Only a few publications report on the development and use of HAP/C composites and, to the best of our knowledge, a comprehensive evaluation of the adsorption properties of HAP/C composites is still missing. In addition, literature lacks a systematic and thorough characterization of composites themselves and a comprehension of how fundamental design parameters, such as carbon content, affect the whole sorption performances of the material.

In this paper, we report on the rational design, synthesis, characterization, and application of eco-friendly HAP/C composites as sorbents for wastewater remediation. The carbonaceous moiety of the composite has been represented by a mesoporous carbon (hereinafter referred to as CMC) already presented in literature [22,23] and obtained from a renewable source (i.e. carbohydrate

biomass). The effect of the CMC content on the structural and morphological properties of the samples have been assessed by means of thermogravimetric analysis (TGA), N_2 adsorption/desorption analyses, electron microscopy (TEM and HAADF-STEM/EDX) analyses, X-ray powder diffraction (XRPD), Fourier-transform infrared (FT-IR), and Raman spectroscopy. In addition, sample surface acidity/basicity measurements have been performed by means of a pulsed acid/base titration method in liquid phase. Batch adsorption tests of simulated wastewater containing benchmark inorganic (Cu(II) and Ni(II)) and organic (Methylene Blue, MB) pollutants have been carried out. The choice of simulated wastewater was dictated by the intention to assess the dual sorption ability of the composites in the absence of complex matrix effects, typical of real industrial effluents. The adsorption kinetics and the effect of initial pollutant concentration and inorganic/organic species co-presence on the overall sorption performance were investigated. Leaching test were also performed to assess the permanent confinement of pollutants.

2. MATERIALS AND METHODS

2.1. Materials

For the synthesis of pristine HAP and/or HAP/CMC composites, aqueous solutions of calcium nitrate tetrahydrate, $Ca(NO_3)_2 \cdot 4H_2O$ (> 99.0%, Merck ACS) and diammonium hydrogen phosphate, $(NH_4)_2HPO_4$ (> 98.0%, Sigma-Aldrich) were used as precursors; an ammonium hydroxide solution, NH_4OH (28–30% wt.%, Fluka) was used for pH adjustment. Details for the CMC synthesis have been reported elsewhere [22,23].

KBr (FT-IR grade, from Sigma-Aldrich) was used to dilute the sample powders for FT-IR analyses.

Liquid-solid acid/base titrations were performed either in cyclohexane (HPLC grade, VWR) or water (HPLC grade, VWR), using 2-phenylethylamine, PEA, (> 99.0%, Sigma-Aldrich) and benzoic acid, BA, (> 99.0%, Carlo Erba) as basic and acid probes, respectively. The samples were packed in

123 a sample-holder column subsequently mounted on an adsorption line; acid-purified powder sea sand
124 (Fluka) and silanized glass wool (Sigma-Aldrich) were used as filling inert materials.

125 Simulated polluted wastewater have been prepared from copper nitrate trihydrate
126 $Cu(NO_3)_2 \cdot 3H_2O$ (>99.5%, Carlo Erba) and nickel nitrate exahydrate $Ni(NO_3)_2 \cdot 6H_2O$ (>99.5%, Carlo
127 Erba) salts and methylene blue, MB (> 99.0 %, Sigma-Aldrich).

128 Lithium hydroxide (purity 99%, Carlo Erba) and oxalic acid (purity ≥ 99%, Sigma-Aldrich)
129 solution was used as eluent in ion chromatographic (IC) analyses, while a solution of 4-(2'-
130 Pyridylazo)-resorcinol free acid (PAR, purity 96%, Sigma-Aldrich) in NH_4OH (purity 30%, Carlo
131 Erba) and acetic acid (pure reagent, Carlo Erba) was used as colorimetric indicator for UV-vis
132 detection of the metal ions. Unless otherwise indicated, all solutions were prepared using MilliQ
133 water (15.2 MΩ, Millipore).

134 *2.2 Synthesis of HAP/CMC composites*

135 HAP/CMC composites were synthesized according to a wet room-temperature (RT) co-
136 precipitation method. Briefly, known amounts of CMC, ranging from *ca*. 300 to *ca*. 1200 mg of CMC
137 (depending on the desired CMC wt.% content) have been dispersed by ultrasonication (15 minutes)
138 in 100 mL of a 0.400 M $(NH_4)_2HPO_4$ solution. The slurry was then placed in a three necked round
139 flask equipped with a mechanical stirrer (central neck). The solution pH was adjusted to *ca*. 9.7 (±
140 0.2) by addition of *ca*. 10 mL of a 28-30 wt.% NH_4OH solution. Then, 100 mL of a 0.668 M
141 $Ca(NO_3)_2 \cdot 4H_2O$ solution was added dropwise by means of a peristaltic pump (1.65 mL min^{-1}). The
142 precursors Ca/P ratio was 1.67 (atom/atom), as to obtain stoichiometric HAP. Precipitation occurred
143 at RT, under mechanical stirring (200 RPM). Periodic additions of ammonia solution were performed,
144 to maintain a constant basic pH. When the addition of the Ca(II) precursor solution was completed,
145 the suspension was stirred for 5 minutes and then vacuum filtered on Buchner funnel. Powders were
146 washed with MilliQ water up to the neutrality of the washing waters, then dried for 16 h at 50°C
147 under vacuum and thermally treated for 8 h at 120°C under air.

148 Following this procedure, four composite materials with different CMC content, namely 4-, 8-,
149 12-, and 16-wt.% (by design) were obtained; such composites will be hereinafter referred to as
150 HAP/CMC4, HAP/CMC8, HAP/CMC12 and HAP/CMC16, respectively.

151 Pristine stoichiometric HAP was synthesized according to the same method but in the absence
152 of the carbonaceous scaffold. For the CMC synthesis, a carbohydrate sample of various origin was
153 added into an aqueous solution of $ZnCl_2$ and heated at 85°C for 3 h, a reaction occurred giving rise
154 to glucose and/or fructose and then hydroxymethyl furfural, with final resinification. The dark-brown
155 viscous resin was cured at 130°C for 1 h to form a black solid. This solid was introduced into a tubular
156 furnace at 450°C for 2 h for the carbonization under flowing N_2 (40 mL/min). The carbonized residue
157 was washed with 1 M HCl and then put in boiling water to remove $ZnCl_2$. The sample was dried at
158 130°C for 6 h. Details can be found in Ref. [22]. Before use, the carbonaceous scaffold was contacted
159 with a NH_4OH containing solution at the same concentration and for the same time used during the
160 composite synthesis, as to represent a proper comparison with the composites themselves.

161 *2.3 Characterization methods*

162 *2.3.1 Structural/morphological characterization techniques*

163 In the following, a brief description of the characterization techniques applied will be given.
164 More detailed information and data interpretation can be found in the Supporting Material.

165 The determination of the CMC content in the composites was performed by TGA analyses
166 (Perkin-Elmer TGA-7) by increasing the sample temperature from 120°C to 800°C at 5°C/min rate
167 under flowing air. Since several phenomena (i.e. decomposition of carbonates and/or release of
168 physically/chemically bound water molecules) could take place in the scanned temperature range, a
169 sort of internal calibration has been performed using *ad-hoc* prepared HAP-CMC physical mixtures
170 with known composition ratio of the pristine HAP and C components. The obtained calibration line
171 is available in the Supporting Material (Fig. S3) together with data of preparation of the physical
172 mixtures (Table S1).

N_2 adsorption-desorption isotherms were collected at liquid nitrogen temperature (-196 °C), by means of a Sorptomatic 1990 version instrument from Thermo Scientific (Carlo Erba). C*a*. 100 mg of each sample, crushed and sieved in 75-180 µm, was used. Surface area (SA) and pore size distribution (PSD) were determined by the 3-parameter BET equation (adsorption branch, $0.005 < p/p^0 < 0.4$) and B.J.H. (Barrett-Joyner-Halenda) model (desorption branch, $0.3 < p/p^0 < 0.95$), respectively.

X-ray powder diffraction analyses were performed using a Philips Powder X-ray diffractometer equipped with a PW 1830 generator. Phase identification was performed by Match! Software, from Crystal Impact GbR.

Transmission electron microscopy (TEM) images were recorded by means of a ZEISS LIBRA 200FE microscope with a 200 kV FEG source equipped with in column second-generation omega filter. Chemical analysis was performed using high angular annular dark field scanning transmission electron microscopy (HAADF-STEM) facility and Energy-dispersive X-ray (EDX) probe (Oxford INCA Energy TEM 200). EDX spectra and element maps were collected along with HAADF-STEM micrographs.

Transmission Fourier Transform Infrared (FT-IR) spectra were collected at RT in the wavenumber range from 400 cm^{-1} to 4000 cm^{-1} by means of a Perkin-Elmer Spectrum Two Fourier transform infrared spectrometer. Wafers of the diluted samples with KBr were prepared (4 mg of sample powder in 200 mg of KBr).

Raman spectra were collected on the sample powder (30-50 mg) using a micro-Raman spectrometer equipped with a Jasco RPM-100 probe, provided with a notch filter and an Olympus 50x objective and interfaced to the laser and to a Lot-Oriel MS125 spectrometer. Spectra have been collected with an acquisition time of 4 s (100 spectra accumulation, background corrected).

2.3.2 Surface acidity/basicity determination

197 Surface acid/basic sites of the studied samples were quantified according to a pulsed-injection
198 titration method described elsewhere [24]. Titrations were performed on a modified HPLC line
199 equipped with a L-6200 A Merck Hitachi pump, a AS-2000A Merck Hitachi autosampler, a L-5025
200 Merck column thermostat and a UV-Visible L-4250 Merck Hitachi detector operating at 254 nm (Fig.
201 *S1* in Supporting Material). 2-phenylethylamine (PEA) and benzoic acid (BA) were used as basic and
202 acid probe molecules, respectively. Titrations were carried out on *ca*. 20 mg of dried sample, crushed
203 and sieved as 80-200 mesh particles, at 30.0 ± 0.1°C in cyclohexane (non-polar aprotic solvent) and
204 in water, as to determine the *intrinsic* and *effective* acidity/basicity of the samples, respectively. A
205 detailed explanation of the method and the calculations performed to quantify the surface sites can be
206 found in the literature [24,25], while a brief one is reported in the Supporting Material (Paragraph
207 S1.2).

208 *2.4 Evaluation of sorption ability of HAP/CMC composites*

209 Adsorption isotherms of individual Cu(II) and Ni(II) onto pristine HAP (*ca.* 100 mg) and of MB
210 onto bare CMC (*ca*. 100 mg) were collected at 30 ± 0.1°C in a broad initial concentration range up
211 to 16,000 ppm, 1200 ppm, and 6000 ppm for Cu(II), Ni(II) and MB, respectively.

212 The sorption ability of pristine HAP and CMC and HAP/CMC composites was evaluated by
213 means of stirred batch adsorption tests. Sorbents (typically *ca*. 100 mg) were placed in test tubes,
214 equipped with magnetic stirrers and contacted with aqueous solutions containing benchmark
215 inorganic (Cu(II) and Ni(II)) and organic (MB) pollutants. Tests were carried out with a constant
216 solid to liquid ratio of 10 $g_{sorbent} \cdot L^{-1}$, at 30.0 ± 0.1°C, with a contact time of 2 hours. Sorption
217 experiments on HAP/CMC composites were carried out varying the initial pollutants concentration
218 in the range from 15 to 300 ppm for individual Cu(II) and Ni(II) containing solutions and from 250
219 to 500 ppm for MB containing ones. Furthermore, the ability of HAP/CMC composites to
220 simultaneously remediate organic and inorganic pollution was evaluated contacting the sorbents with

ternary Cu(II)-Ni(II)-MB solutions with initial concentrations of 300 ppm for both cations and 250 ppm for the organic dye; the pH value of all solutions was 5.5 (± 0.5).

At the end of the sorption tests, supernatants were collected, properly diluted when necessary, and then analyzed to determine the residual concentration of pollutant species. Quantification of the initial and final Cu(II) and Ni(II) concentrations have been carried out by means of ionic chromatography (Dionex DX-120 chromatograph equipped with a Dionex IonPacTM CS5A 4 x 250 mm column, derivatization system with PAR solution and a Merck Hitachi L-4200 UV/Vis detector). Initial and final MB concentration were instead determined by UV-visible spectrophotometry (Shimadzu UV–3600 spectrophotometer) at fixed wavelength λ_{max} = 662 nm (a calibration curve in the linear range 1-50 mg L^{-1} was prepared for determining the extinction coefficient $\varepsilon_{662}^{25°C} = 0.195 \pm 0.005$ L · $mg^{-1} \cdot cm^{-1}$).

The adsorption capacity of sorbents towards pollutants was quantified in both percentage of species removal and in pollutant loaded mass on sorbent mass ($mg_{pollutant} \cdot g_{sorbent}^{-1}$), according to the following equations:

$$Percent\ removal\ (\%) = \frac{C_i - C_f}{C_i} \times 100 \qquad \textit{Equation 1}$$

$$Uptake\ capacity\ \left(mg_{pollutant} \cdot g_{sorbent}^{-1}\right) = \frac{(C_i - C_f) \times V_{sol}}{m_{sorbent}} \qquad \textit{Equation 2}$$

where C_i and C_f are the initial and final concentration of pollutant in ppm (mg L^{-1}), V_{sol} is the volume of simulated wastewater contacted with the sorbent (L) and $m_{sorbent}$ is the actual mass of sorbent in the test tube (g).

The effect of sorbent dosage was investigated as well, following the same batch adsorption procedure. Specifically, 2 hours-long adsorption tests in ternary mixtures, Cu(II)-Ni(II)-MB mixtures, were carried out with different dosages on selected composites, ranging from 0.5 to 25 $g_{sorbent} \cdot L^{-1}$ and initial concentrations of Cu(II) and Ni(II) of 300 ppm, each, and of MB of 250 ppm.

Adsorption kinetics in ternary Cu(II)-Ni(II)-MB mixtures were studied following the above-described batch adsorption procedure under stirring, operating with initial concentrations of Cu(II) and Ni(II) of 300 ppm each, and of MB of 250 ppm, monitoring the supernatant Cu(II), Ni(II) and MB concentration at successive intervals of contact time, up to 2 hours.

Modeling of experimental kinetic data was carried out using the Runge-Kutta based Excel user interface provided by Wang et al [26]. Three adsorption reaction models, namely pseudo-first-order (PFO, Equation 3), pseudo-second-order (PSO, Equation 4) and Elovich (Equation 5) models, have been applied in their non-linear forms herein reported:

$$q_t = q_e(1 - e^{-k_1 t}) \qquad \textit{Equation 3}$$

$$q_t = \frac{q_e^2 k_2 t}{1 + q_e k_2 t} \qquad \textit{Equation 4}$$

$$q_t = \frac{1}{b}\ln(1 + abt) \qquad \textit{Equation 5}$$

where:

- q_t: Adsorbed amount of adsorbate at time t ($mg_{adsorbate} \cdot g_{sorbent}^{-1}$);
- q_e: Adsorption capacity at equilibrium ($mg_{adsorbate} \cdot g_{sorbent}^{-1}$);
- t: Time (min)
- k_1: Pseudo-first-order rate constant (min^{-1});
- k_2: Pseudo-second-order rate constant ($g_{sorbent} \cdot mg_{adsorbate}^{-1} \cdot min^{-1}$);
- a: Initial adsorption rate constant of the Elovich model ($mg_{adsorbate} \cdot g_{sorbent}^{-1} \cdot min^{-1}$);
- b: Energetic/surface coverage Elovich parameter ($g_{sorbent} \cdot mg_{adsorbate}^{-1}$).

Time-dependent adsorption rate according to Elovich adsorption model equation has been calculated applying the derivative form of Elovich equation (Equation 6) itself:

$$Elovich\ ads.rate = \frac{dq_t}{dt} = ae^{-bq_t} \qquad \textit{Equation 6}$$

Leaching tests were carried out on selected pollutant-loaded samples. After adsorption batch tests, the solids were separated from the solution and dried at 120°C for 16 hours before they

underwent leaching tests. *Ca*. 0.1 g of loaded sample was suspended in 10 mL of MilliQ water (pH *ca*. 5) and stirred for 24 hours at RT. The release of pollutants from used sorbents have been quantitatively evaluated by means of the same above-described analytical techniques.

3. RESULTS AND DISCUSSION

3.1 Characterization of HAP/CMC composites

3.1.1 Composition, structure and morphology

Four HAP/CMC composites with different CMC content (ranging from 4 to 16 wt.%) were prepared as described in paragraph 2.2.

First, the effective CMC content in all composites was determined by means of TGA experiments. Indeed, determining the weight loss ascribable to CMC combustion allows estimating the amount of CMC in the samples. Fig. ***1*** comparatively shows the collected thermogravimetric profiles of the HAP/CMC composites (black lines) and the homo-compositional HAP-CMC physical mixtures (red lines), the latter used as references to properly correlate samples weight loss with effective CMC content (calibration line available in the Supporting Material, Fig. S3).

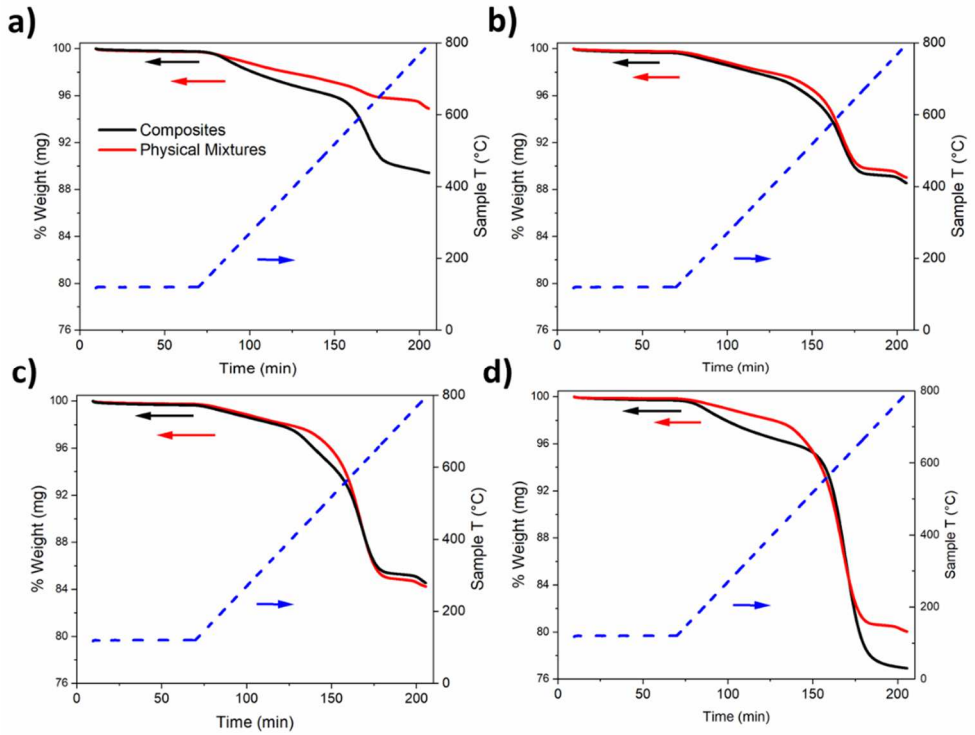

283

284 **Fig. 1**. Thermogravimetric profiles of HAP/CMC4, a); HAP/CMC8, b); HAP/CMC12, c); and
285 HAP/CMC16, d) composites (black lines) and of the related HAP-CMC physical mixtures (red lines)
286 as functions of time and temperature of analysis.

287

288 A major thermal phenomenon, addressable to CMC combustion, takes place in the temperature
289 range between 400 and 650°C for all samples. Combustion reaches its maximum rate, identified by
290 the inflection point in the thermogravimetric profile, at *ca*. 585°C. Making use of the calibration line
291 obtained from the TG analyses of physical mixtures, the actual CMC content of each composite was
292 evaluated. The results, collected in the second column of Table 1, show an experimentally determined
293 CMC content slightly higher than that predicted by design. A moderate mass loss occurs prior to the
294 triggering of CMC combustion; the temperature range (120°C < T < 400°C) and the overall slow
295 kinetics of the phenomenon are consistent with thermal decomposition of surface and/or bulk HAP
296 carbonate species, as already observed in other synthetic hydroxyapatite samples [27].

297 **Table 1.** Compositional, morphological and acid-base surface properties of pristine HAP and CMC components and HAP/CMC composites.

Sample	CMC content[a]	Surface Area[b]	HAP/CMC		Porosity range[e]	Pore Volume	Acid sites[f]		Basic sites[f]	
	wt. %	m^2g^{-1}	*mass*[c]	*surface area*[d]	*nm*	$cm^3\ g^{-1}$	*meq* g^{-1}	$\mu eq\ m^{-2}$	*meq* g^{-1}	$\mu eq\ m^{-2}$
HAP	0	101	-	-	2.9 – 6.7	0.306	0.221	2.197	0.016	0.156
HAP/CMC4	6.16	137	15.23	1.24	2.0 – 2.9	0.258	0.156	1.139	0.004	0.030
HAP/CMC8	8.37	130	10.95	0.89	2.0 – 3.9	0.221	0.089	0.687	0.006	0.048
HAP/CMC12	12.95	149	6.72	0.55	2.0 – 3.9	0.224	0.091	0.613	0.020	0.137
HAP/CMC16	19.60	129	4.10	0.33	1.0 – 4.8	0.113	0.021	0.174	0.003	0.024
CMC	100	1236	-	-	1.0 – 2.9	1.18	0.251	0.203	0	0

298 [a] *Determined by TGA analyses;*

299 [b] *Evaluated by 3-parameters BET equation;*

300 [c] *Mass ratio calculated as:* $\frac{m_{HAP}}{m_{CMC}} \times 100$*;*

301 [d] *Surface area ratio calculated as:* $\frac{m_{HAP} \times SA_{HAP}}{m_{CMC} \times SA_{CMC}} \times 100$*;*

302 [e] *Range of pore size covering the 75% of the total pore volume;*

303 [f] *Intrinsic values, determined by pulsed-injection method in cyclohexane at 30°C. Probe molecules: PEA, for acid site- and BA, for basic site-*
304 *determination.*

Surface area and pore size distributions on pristine HAP, CMC and HAP/CMC composites have been investigated by measuring N_2 adsorption/desorption isotherms. Results have been collected in Table 1 ~~and~~ while the adsorption/desorption isotherms and pore size distributions (PSD) of the pristine moieties and HAP/CMC8 are reported in Fig. 2. All isotherms and PSD are instead available in the Supporting Material (Fig. S4 and S5).

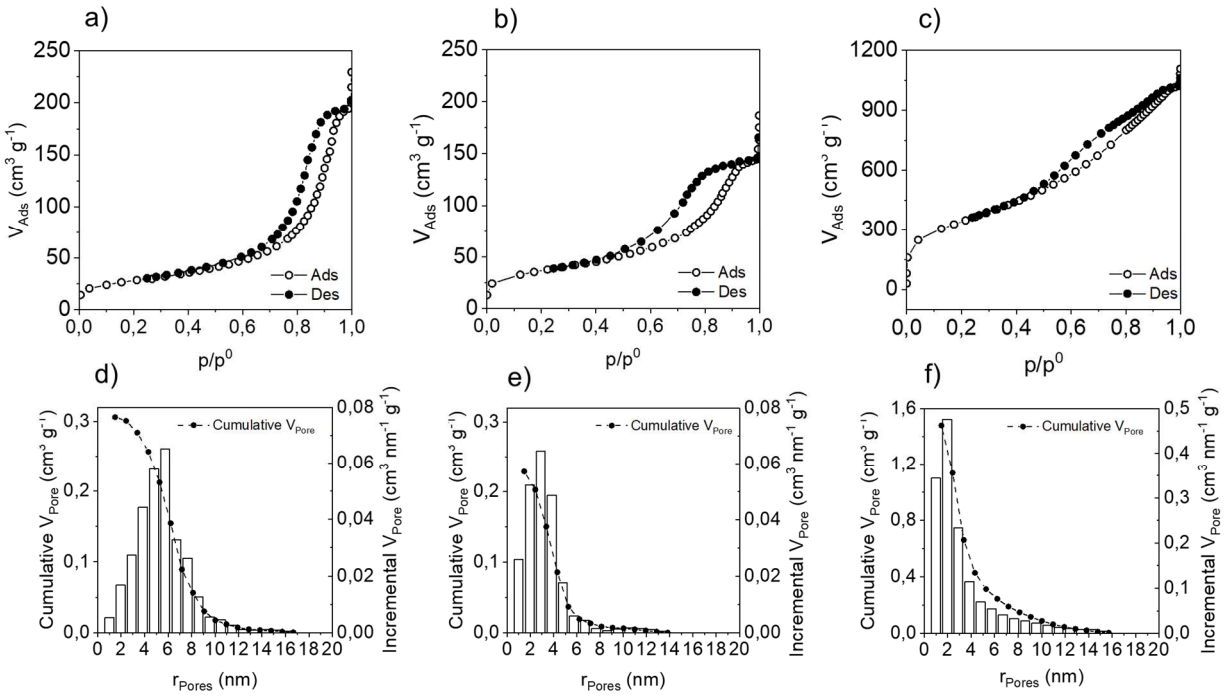

Fig. 2. N_2 adsorption/desorption isotherms and pore size distributions (BJH method, $0.3 < p/p^0 < 0.95$) of pristine HAP, a) and d, HAP/CMC8 composite, b) and e); and pristine CMC, c) and f).

Both pristine moieties and composites exhibit type IV isotherms (according to the IUPAC classification)~~,~~ typical of mesoporous materials. On the other hand, differences can be spotted in the desorption hysteresis. Indeed, pristine HAP and HAP/CMC composites up to HAP/CMC12 exhibited a H2 type hysteresis, which indicates mesopores of not-well defined shape. Conversely, CMC and composite HAP/CMC16 showed H4 hysteresis, suggesting the slight presence of micropores in addition to the assessed mesoporosity. Such microporous contribution for CMC and HAP/CMC16 is further confirmed by the PSD (Fig. 2 and Fig. S5 in Supporting Material).

Pristine HAP and CMC have different surface area values, with a *ca*. one order of magnitude larger SA for CMC; both mass and surface area ratios of HAP/CMC composites have been calculated and reported in Table 1. Obtained values indicate that, the mass ratios between HAP and CMC in the composites, which are dominated by HAP, are confined in a narrower interval than surface area ratios, the latter spanning from 0.33 (carbon-rich surfaces) to 1.24 (hydroxyapatite-rich surfaces). Although no clear trend of the surface area values of composites against CMC content can be spotted, an unexpected general decrease of the HAP/CMC surface ratios could be noticed. The pore size distributions of composites indicate a transition from a HAP-like mesoporous morphology (up to ca. 12% CMC addition) to a CMC-like one, in which microporosity dominates. The marked decrease of pore volume, passing from the CMC sample to HAP/CMC composites, suggests that pore clogging and/or CMC pore filling with the hydroxyapatitic moiety likely occurred during the disordered precipitation of HAP onto the carbonaceous scaffold. Such phenomena might explain the limited values of surface area exposed by the composites in comparison to the expected values.

The collected XRPD patterns of the samples (Fig. 2) revealed for CMC a predominant amorphous nature. The typical 002 and 101 reflections of graphite [28] are detected in the form of two broad peaks in the regions between 20°-30° and 40°-45° in 2θ, respectively. Large full width at half maximum of the peaks suggests that CMC possesses a disordered structure, composed of small and randomly stacked hexagonal aromatic sheets [23]. In composites, the XRD pattern of crystalline HAP was clearly observed (Fig. 3); the overall broadening and simultaneous reduction of intensity of the HAP peaks as the CMC content increased indicated a progressive decrease in the crystallinity of the samples.

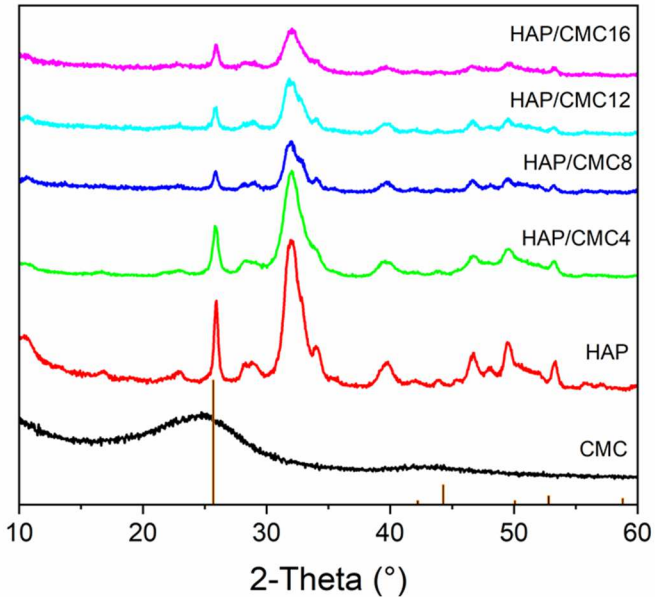

342

343 **Fig. 3.** XRPD patterns of pristine HAP and CMC moieties and HAP/CMC composites (brown bars
344 indicate the expected contributions of graphite reflections).

345

346 TEM images of HAP/CMC composites are collected in Fig. 4 and those of pristine materials in
347 Fig. S6. CMC exhibits a disordered sponge-like structure, as already reported in the literature [22,
348 23] while pristine HAP has an irregularly shaped morphology, forming nanoplatelets of ca. 5x40 nm
349 dimensions (Fig. S6). Concerning the composites, for low CMC content (up to 12 wt.%) the
350 morphologic features are dominated by HAP, being HAP crystallites partially covered by amorphous
351 layers of CMC (Fig. 6a and 6b). Increasing CMC content (HAP/CMC16, Fig. c) a transition towards
352 the CMC-morphology was clearly observed. The present observation is consistent with the
353 morphological transition already discussed on the surface area and porosity results of the composites.

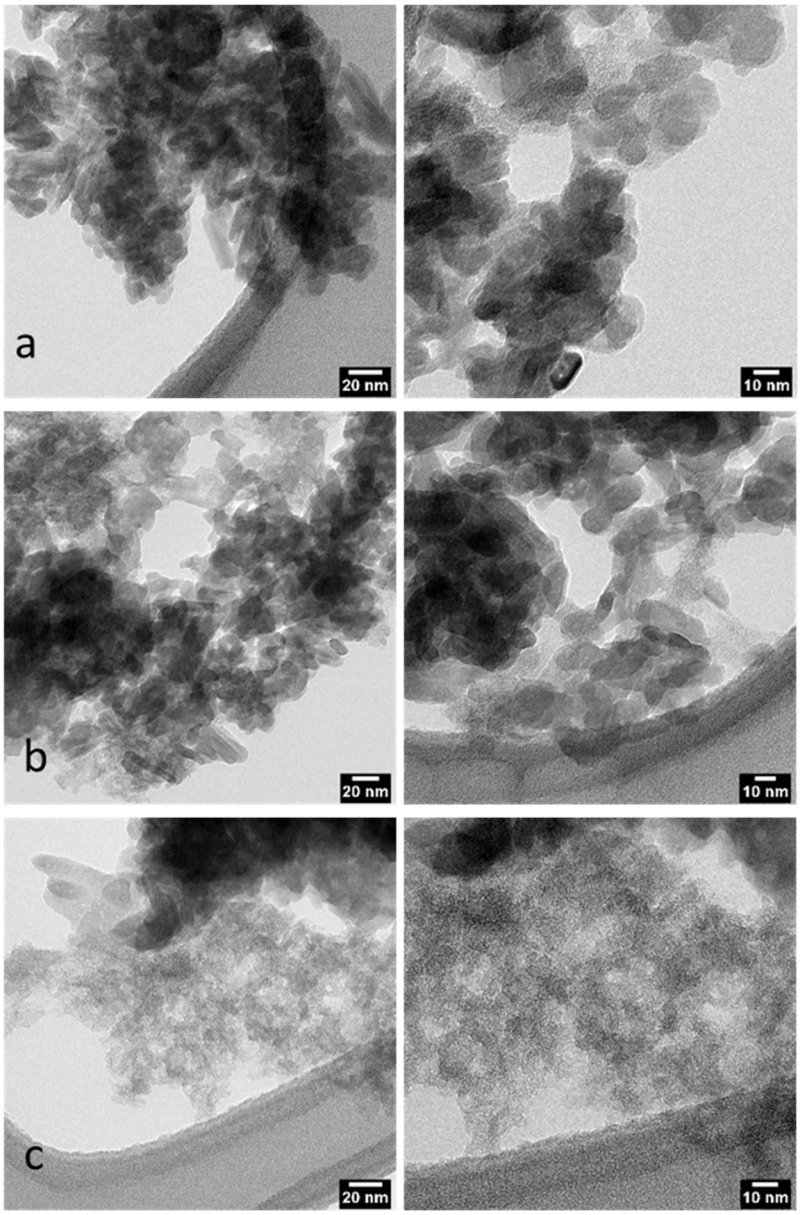

Fig. 4. TEM images of HAP/CMC8, a); HAP/CMC12, b); and HAP/CMC16, c) at two magnifications: 20 nm (left) and 10 nm (right).

The HAP/CMC composites were also investigated by HAADF-STEM microscopy and HAADF-STEM /EDX maps. The investigated area of HAP/CMC8 appears homogeneous in composition with a distribution of the P, Ca and C elements consistent with the co-presence of the HAP and CMC phases (Fig. 5a). HAADF-STEM/EDX maps of the samples with increasing CMC content (HAP/CMC12 and HAP/CMC16, Fig. 5 b and 5 c) show increasing presence of carbon phase. In particular, the atomic map of HAP/CMC16 shows regions with carbon phase in contact with

hydroxyapatite (Ca/P ≈1.3) besides separate C-phase (Fig. 5c). This evidence supports the already discussed changes in sample morphology with increasing CMC content.

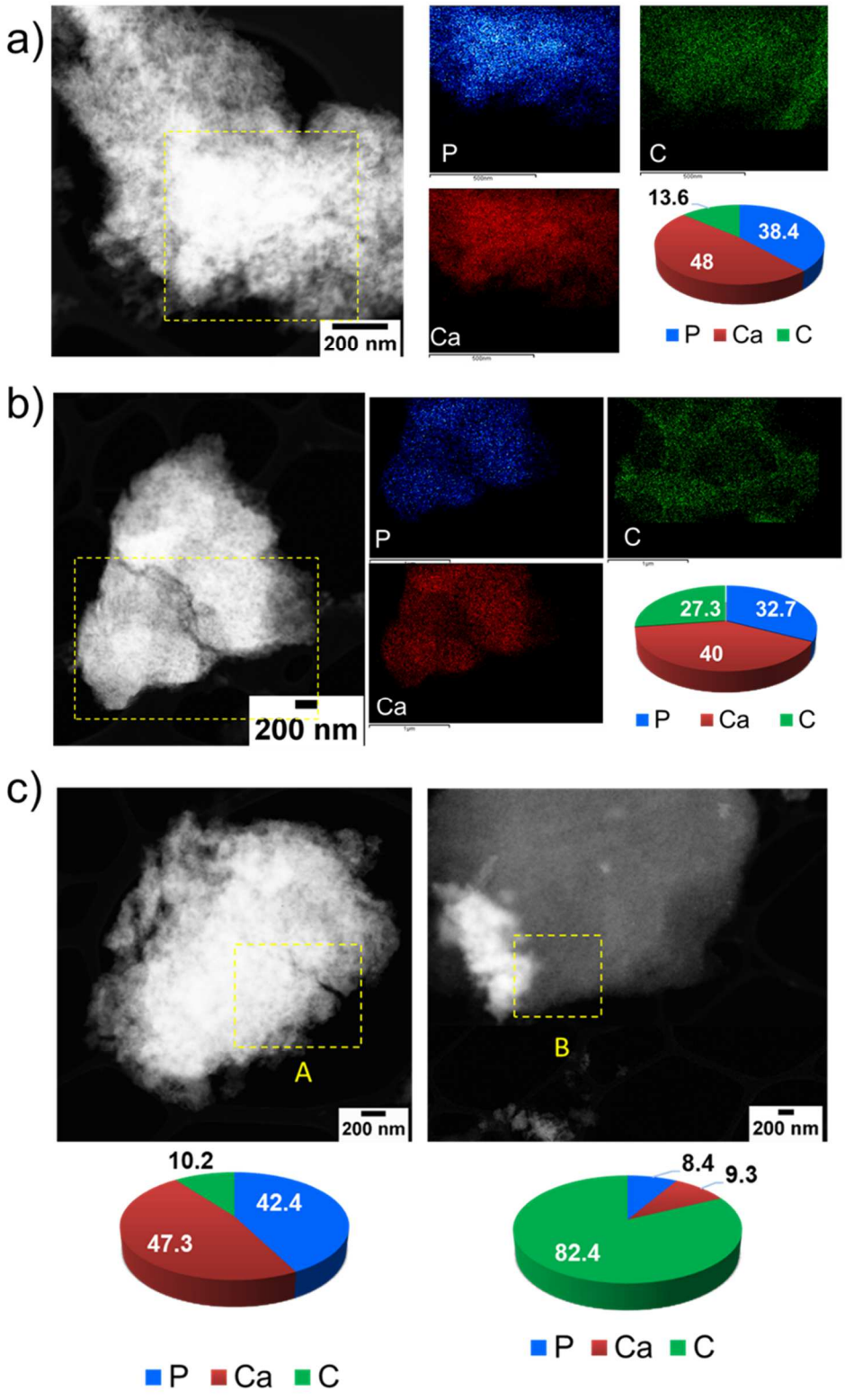

Fig. 5. HAADF-STEM micrographs and HAADF-STEM/EDX mapping of P, Ca, and C (normalized values) on HAP/CMC8, a); HAP/CMC12, b); and HAP/CMC16, c) samples.

370 *3.1.2 Surface properties*

371 Transmittance FT-IR spectra of all the studied samples were collected to have further information
372 on the surface functional groups. All the spectra can be found in Fig. S.

373 Although the typical low transmittance of (black) carbon-containing materials did not allow
374 quantitative considerations, a meaningful insight on the surface functional groups of composites could
375 be provided by this technique. The CMC infrared spectrum showed four broad contributions in four
376 different IR regions. Such signals could be assigned to (*i*) stretching mode of O-H (*ca*. 3404 cm^{-1}),
377 (*ii*) stretching mode of C=O (*ca*. 1700 cm^{-1}), (*iii*) stretching mode of conjugated C=C aromatic bonds
378 (*ca*. 1571 cm^{-1}) and (*iv*) stretching mode of C-O groups of esters/alcohol functionalities (*ca*. 1264 cm^{-1}
379) [22]. Interestingly, the contribution of C-H stretching at *ca*. 2930 cm^{-1} was not detected, thus
380 indicating a highly functionalized carbon with limited C-H terminal groups, at the advantage of O-
381 functionalized terminations. The present results are consistent with the relevant surface oxygen
382 content (*ca*. 7.4 at.%) and nature of oxygenated surface groups of CMC, as reported in previous
383 studies [23].

384 HAP infrared spectrum showed the typical apatite contributions. Attention has been directed to
385 two regions: (*i*) a broad band between 3500 and 3300 cm^{-1}, ascribable to O-H stretching modes of
386 constitutive/surface bond water molecules, together with a sharp contribution of O-H stretching of
387 structural basic hydroxyl groups at 3570 cm^{-1} and (*ii*) two low energy bands between 1100 and 500
388 cm^{-1}, associated to the fundamental vibration modes of phosphate groups (Fig. S). No carbonates
389 contributions were detected in the typical infrared region (1600 to 1350 cm^{-1}), suggesting that the
390 synthetic route employed minimizes the incorporation of CO_3^{2-} groups in the HAP lattice, although
391 they are common surface compositional impurities found in HAP obtained by wet co-precipitation
392 methods [27]. It could be guessed that the high concentration of precursor solutions (i.e. high ionic
393 strength) and fast addition rate of the Ca-containing solution (i.e. short synthetic time) partake in
394 decreasing the quantity of carbonates available for incorporation in HAP lattice.

Spectra of all HAP/CMC composites always displayed the typical infrared signals of HAP. Interestingly, the carbonates bands, not detected on pristine HAP, are clearly visible in HAP/CMC4 spectrum (Fig. S); such contribution is allegedly present in all the composites up to HAP/CMC16 although the continuous decrease of infrared transmittance of the samples (in consequence of the increase in CMC content) made it difficult to properly assess their presence.

Raman spectra (Supporting Material, Fig. S) were also collected on composites and pristine moieties, as to complete the qualitative survey of composite surface. Consistently with its carbonaceous nature, pristine CMC (Fig. Sa) shows the typical G (graphite in plane E_{2g} Raman active mode, given by ordered domains) and D (A_{1g} D breathing mode, from disordered domains) bands at *ca*. 1530-1620 cm^{-1} and *ca*. 1350 cm^{-1}, respectively. The I_D/I_G ratio of pristine CMC (≈ 0.8) indicates a mostly amorphous material with moderate presence of small graphitic domains, in the order of *ca*. 1 nm of size [29]. Therefore, Raman characterization agrees with the previously discussed XRPD results. The Raman spectrum of pristine HAP (Fig. Sb) is instead characterized by a high-intensity semicircular pattern typical of phosphorescence phenomena, hampering the collection of any information on the material.

HAP/CMC composites spectra exhibit G and D bands at the same Raman shift and an I_D/I_G ratio close to the former 0.8, confirming the carbonaceous scaffold is unaltered by compositing. Interestingly, a signal at *ca*. 961 cm^{-1} is detected in HAP/CMC4 and HAP/CMC8 samples; such peak is commonly attributed to the ν_3 symmetric stretching mode of PO_4^{3-} groups [30]. The detection of this contribution at low CMC content and its disappearance at CMC content > *ca*. 8 wt.% may indicate a lower surface exposure of phosphate groups (i.e. HAP moieties) when the HAP/CMC surface area ratio is << 1.

3.1.3 Surface acidity and basicity

The number of acid and basic surface sites of pristine moieties and HAP/CMC composites have been determined according to a pulsed-injection acid-base titration method. Fig. shows the trend of

420 the surface density of the *intrinsic* acid and basic surface sites (i.e. titrated in cyclohexane, a non-
421 polar and aprotic solvent) against the CMC concentration in the HAP/CMC composites. The extreme
422 points of the graph correspond to pristine HAP and CMC. The obtained results are collected in Table
423 1.

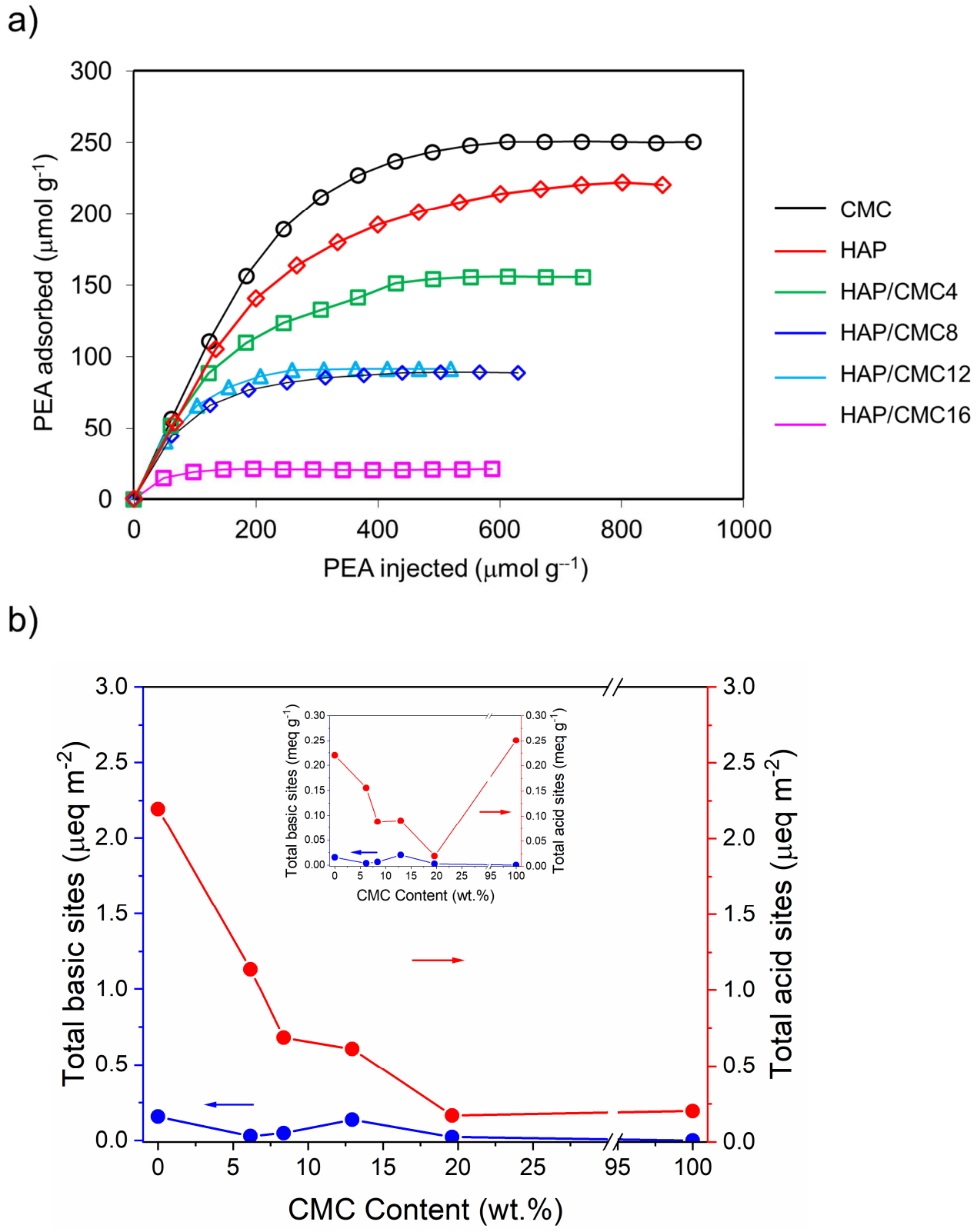

Fig. 6. Acidity results obtained by PEA titration at 30°C on the pristine moieties and HAP/CMC composites, a); trends of the intrinsic surface basicity (left axis) and acidity (right axis) of the pristine moieties and HAP/CMC composites reported as a function of CMC concentration (in percent), b). Inset reports the same results expressed as meq·g^{-1}.

The density of surface acid sites (right axis of Fig. b) decreases almost hyperbolically passing from pristine HAP to pristine CMC, the latter exhibiting the lowest density of the series as a consequence of its one order of magnitude larger surface area (Table 1). Indeed, when the number of acid sites is plotted as a function of sample mass (meq·g^{-1}, inset in Fig. b), it can be noticed that CMC effectively possesses a large number of acid surface sites, mainly constituted by -COOH surface groups. The overall acidity of CMC sample was lower than what reported in previous studies [21] because of the basic treatment suffered in this study (see paragraph *2.2 Synthesis of HAP/CMC composites*). The decrease of the density of acid sites for increased CMC concentration in the composites is consistent with the slight increase of the surface area in respect to pristine HAP and it is coherent with the increasing share of carbonaceous surface exposed. The number/density of the surface acid sites of pristine HAP reported in Table 1 is in agreement with the literature values (2.197 μeq·m^{-2} vs. 1.871 μeq·m^{-2} reported in [18]); the small discrepancy is addressable to (*i*) the slightly different synthetic route for HAP and (*ii*) the different acid-base titration technique (pulsed-injection method vs. LRCM) employed for the quantification of acid surface sites.

Basic sites density (left axis of Fig. b) was barely detectable in both pristine moieties and throughout the whole composition range of composites. If negligible basicity could be envisaged for CMC because of its acidic and carbonaceous nature [21], an unexpectedly low number/density of basic sites was obtained for pristine HAP (0.156 μeq·m^{-2} vs. 2.341 μeq·m^{-2} reported in [14]). Concerning the basicity of HAP/CMC composites, HAP/CMC12 slightly deviates from the observed trend, although in absolute value the measured density of basic sites is always low (< 0.150 μeq·m^{-2}). The results might indicate a low number/density of strongly interacting basic sites at the HAP surface (and consequently, on all HAP/CMC composites surface as well). Nonetheless, it should be taken into account that the sluggish adsorption kinetics of BA onto the surface basic sites (see discussion in the Supporting Material, paragraph S1.1 and typical chromatograms obtained, Fig. S2) and the high flowrate of the carrier solvent might lead to an underestimation of the number of basic

456 sites. Furthermore, it can be hypothesized that basic sites of HAP are not exposed to the open surface
457 of HAP but allocated in the channels where it is hard to contact them.

458 The *effective* number/density of acid and basic surface sites measured in water of pristine
459 moieties and composites is reported in the Supporting Material (Table S2). In water, neither *effective*
460 acidity nor basicity of any other sorbent than CMC could be titrated. The difficulty in determining
461 *effectiv*e surface properties is addressed to the polarity and proton donor/acceptor nature of water
462 itself, which may be strongly adsorbed by acid and basic surface groups and hardly displaced by the
463 probe molecules, thus hampering the titration. In the specific case of CMC, the retention of surface
464 acidity (0.240 $\mu eq \cdot m^{-2}$, almost equal to the intrinsic value of 0.204 $\mu eq \cdot m^{-2}$, Table 1) may be addressed
465 to the hydrophobicity of the material, which prevent water to fully interact with the surface acidic
466 groups.

467 *3.2 Sorption ability of HAP/CMC composites*

468 *3.2.1 Sorption of individual organic/inorganic polluting species*

469 HAP/CMC composite ability to remove hazardous pollutants have been evaluated in simulated
470 wastewaters individually containing Cu(II), as benchmark heavy metal pollutant species, Ni(II), as
471 representative of emerging inorganic pollutant detectable in electrical industries effluents [17], and
472 MB, as a typical organic pollutant.

473 At first, maximum adsorption capacity of bare HAP and CMC towards inorganic (Cu(II) or
474 Ni(II)) and organic (MB) benchmark pollutants have been respectively evaluated collecting
475 adsorption isotherms at 30°C. The adsorption isotherms of individual Cu(II) and Ni(II) onto HAP and
476 of MB on CMC are reported in Fig. 7.

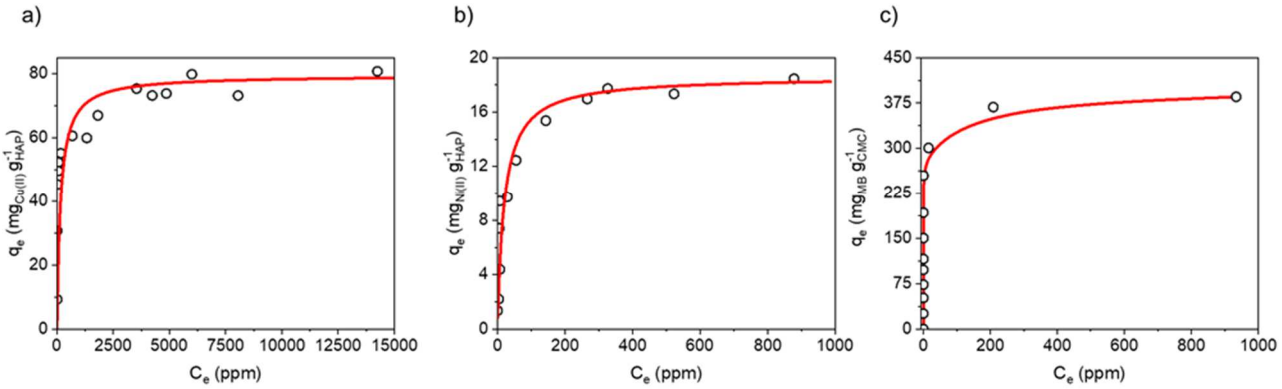

477

478 **Fig. 7.** Adsorption isotherms, collected at 30°C according to the stirred batch adsorption method for
479 Cu(II), a) and Ni(II), b) onto pristine HAP and for MB, c) onto bare CMC (Ni(II) adsorption isotherm,
480 already published [17], is reported for the sake of clarity).

481

482 In the case of metal ion adsorption by hydroxyapatite, the isotherms showed sharp inflection (knee)
483 from which a near horizontal portion starts, asymptotically approaching a ceiling value corresponding
484 to the saturation of the HAP surface with the metal species. These isotherms curves could be well
485 modelled by the Langmuir equation (Table 2). It is evident the higher affinity of HAP for Cu(II) ions
486 (*ca*. 80 $mg \cdot g^{-1}$) compared to Ni(II) (ca. less than 20 $mg \cdot g^{-1}$). The preferential adsorption of Cu(II) over
487 Ni(II) is consistent with previous data reported in the literature by our group [17,31] and other authors
488 [14]. Considering that both Cu(II) and Ni(II) have been demonstrated to be immobilized onto the
489 HAP essentially by surface complexation mechanism [17,31], the different affinity of the surface
490 groups of HAP (namely -OH, -POH and, eventually, -COH) towards Cu(II) and Ni(II) species could
491 justify the observed discrepancy in the cation maximum adsorption capability. Actually, by
492 comparing the complexation constants of analogous aqueous complex (i.e metal-phosphate, metal-
493 hydroxyl and metal carbonate complexes) for Cu(II) and Ni(II), the higher stability and interaction
494 strength of copper complexes compared to those involving Ni(II) clearly emerged (Table S3).
495 The MB adsorption isotherm on CMC showed an almost vertical initial part of the experimental curve
496 (the portion before the knee); this profile, classified as H-isotherm [32,33], is a special case of the
497 Langmuir isotherm, occurring when adsorbate has such high affinity towards the sorbent that in dilute

498 solutions it is quantitatively retained. In this case, the first part of the isotherm can be modelled by
499 the Henry's isotherm. The high affinity of CMC towards MB is confirmed by the remarkable
500 maximum adsorption capacity (ca. 400 $mg \cdot g^{-1}$).

501 **Table 2.** Maximum adsorption capacities of HAP and CMC towards inorganic and organic
502 pollutants

Pollutant species	**Sorbent**	**Adsorption model equation**	**Maximum ads. capacity (q_e)** $mg_{pollutant} \cdot g^{-1}{}_{HAP}$
Cu(II)	HAP	Langmuir	79.5 ± 1.2
Ni(II)	HAP	Langmuir	18.6 ± 0.2
MB	CMC	Henry / Empirical	≈ 380 ± 10

503

504 Table 2 demonstrate that pristine HAP and CMC are efficient sorbents for inorganic and organic
505 polluting species, respectively, displaying complementary adsorption features.

506 Then, HAP/CMC composite ability to remove individual pollutants were evaluated by means of
507 stirred batch adsorption tests at different initial pollutant concentration. In Table 3, the remediation
508 performances shown by HAP/CMC composites are reported. In the Supporting Material (Fig. S and
509 Fig. S6), the same data have been graphically displayed.

Table 3. Adsorbed inorganic pollutants by pristine moieties and HAP/CMC composites.[a]

Sample	Individual pollutant species								Simultaneous pollution		
	Adsorbed Cu(II) $mg_{Cu(II)} \cdot g^{-1}_{sorbent}$			Adsorbed Ni(II) $mg_{Ni(II)} \cdot g^{-1}_{sorbent}$			Adsorbed MB $mg_{MB} \cdot g^{-1}_{sorbent}$		Cu(II) $mg_{pollutant} \cdot g^{-1}_{sorbent}$	Ni(II)	MB
	$C_0 \approx 15$ ppm	$C_0 \approx 75$ ppm	$C_0 \approx 300$ ppm	$C_0 \approx 15$ ppm	$C_0 \approx 75$ ppm	$C_0 \approx 300$ ppm	$C_0 \approx 250$ ppm	$C_0 \approx 500$ ppm	$C_0 \approx 300$ ppm	$C_0 \approx 300$ ppm	$C_0 \approx 250$ ppm
HAP	1.53 *(98.1%)*[b]	7.93 *(99.6%)*	32.02 *(99.8%)*	1.45 *(88.5%)*	5.85 *(70.0%)*	10.53 *(42.3%)*	3.91 *(16.9%)*	6.44 *(13.5%)*	29.76 *(98.6%)*	7.34 *(27.0%)*	0.64 *(2.8%)*
HAP/CMC4	1.55 *(98.7%)*	8.01 *(99.7%)*	26.66 *(98.6%)*	1.34 *(88.2%)*	6.34 *(76.1%)*	14.36 *(44.7%)*	20.09 *(80.8%)*	25.59 *(52.8%)*	28.55 *(95.4%)*	7.77 *(28.8%)*	21.62 *(93.7%)*
HAP/CMC8	1.59 *(99.6%)*	7.87 *(99.8%)*	30.43 *(98.4%)*	1.40 *(89.8%)*	6.18 *(76.4%)*	11.42 *(37.2%)*	24.83 *(100%)*	37.95 *(78.6%)*	29.29 *(93.1%)*	7.37 *(26.0%)*	24.10 *(99.4%)*
HAP/CMC12	1.39 *(99.7%)*	6.33 *(99.8%)*	30.23 *(98.5%)*	1.45 *(89.6%)*	6.50 *(80.1%)*	13.13 *(40.0%)*	24.58 *(100%)*	40.95 *(88.9%)*	30.13 *(96.3%)*	4.72 *(17.2%)*	24.12 *(99.9%)*
HAP/CMC16	1.56 *(99.5%)*	5.99 *(99.6%)*	29.23 *(96.4%)*	1.37 *(90.1%)*	5.55 *(78.4%)*	9.74 *(29.0%)*	25.06 *(100%)*	47.36 *(99.7%)*	28.75 *(91.5%)*	3.78 *(14.1%)*	24.17 *(99.8%)*
CMC	1.52 *(100%)*	6.48 *(85.5%)*	12.21 *(39.4%)*	1.67 *(100%)*	5.00 *(65.1%)*	6.49 *(20.1%)*	25.06 *(100%)*	48.78 *(100%)*	15.33 *(46.9%)*	2.68 *(9.1%)*	25.21 *(99.9%)*

[a] *Sorption tests performed according to a stirred batch method, T = 30°C, contact time = 2 h, pH 5.5 (± 0.5).*

[b] *Percentage removal calculated on the initial amount of pollutant in solution. All percentage data reported in the Table are affected by ca. ±2% error.*

513 Table 3 indicates an almost complete removal of Cu(II) by all HAP/CMC composites, stemming
514 from the pronounced affinity of HAP with this cation [14,31,34], which is in turn confirmed by the
515 sorption performance of pristine HAP itself (Fig. 7a and 7b).
516 On the opposite, pristine CMC is characterized by a limited sorption ability towards Cu(II),
517 exhibiting a *ca*. 40% removal when Cu(II) initial concentration was 300 ppm. The recognized low
518 affinity of activated carbons for cations adsorption and the almost null amount of (basic) surface
519 effective functionalities of CMC [35] are supposed to determine such negative performances. In a
520 similar fashion, Ni(II) adsorption ability of HAP/CMC composites (Table 3) is consistent with the
521 pristine HAP ability towards Ni(II); a slight decrease in removal performance can be spotted for
522 increasing CMC content when the initial concentration of the pollutant was higher than 75 ppm. Apart
523 from these considerations on HAP/CMC composites, Ni(II) confirms to be hardly adsorbed on usually
524 efficient low-cost sorbents like HAP [14–16].
525 Regarding MB, HAP sorption capacity towards this organic pollutant is modest, as expected from
526 literature [20]. Conversely, CMC fully immobilizes the dye, mainly thanks to the peculiar ability of
527 carbonaceous materials to establish π–π interaction with molecules bearing aromatic rings [20,36].
528 Notwithstanding the low CMC content, the HAP/CMC composites possess excellent sorption
529 properties towards MB. The HAP/CMC16 sample ensured total removal of the species under both
530 testing conditions, while an amount of CMC corresponding to *ca*. 8 wt.% content was sufficient to
531 completely remediate MB pollution when its initial concentration was 250 ppm. The relatively low
532 amount of CMC in composites guaranteed fast and effective sorption of MB, retaining the peculiar
533 CMC sorption features despite the compositing with HAP.

534 *3.2.2 Simultaneous removal of organic and inorganic pollutants*

535 After assessing the ability of HAP/CMC composites to adsorb individually both inorganic and
536 organic pollutants, the sorbents performances were evaluated contacting them with ternary solutions,
537 containing 300 – 300 – 250 ppm of Cu(II), Ni(II) and MB, respectively (Table 3 and Fig. S7).

538 The results obtained for pristine HAP and CMC confirmed the complementary adsorption ability
539 of the two moieties, already observed. HAP displayed an optimal adsorption capacity towards the
540 inorganic species (almost full removal of Cu(II) and *ca*. 26% removal of Ni(II)) while CMC exhibits
541 outstanding ability in trapping MB. Interestingly, the high affinity of hydroxyapatite towards Cu(II)
542 ions resulted in preferential adsorption of this species at the expense of Ni(II) ions. Differently, the
543 performances of CMC are not varied, except for Ni(II) uptake, which also in this case suffers from
544 the co-presence of MB and Cu(II).
545 The dual nature of HAP/CMC composites conferred them unique adsorption capacity towards both
546 organic and inorganic pollutants. In particular, Cu(II) was trapped on HAP/CMC composites with a
547 removal efficiency ranging from 85 to 95% throughout the whole range of CMC content studied,
548 evidencing that the diminished amount of HAP moiety in the composite did not affect the uptake of
549 this metal species. On the other hand, Ni(II) removal percentage decreases from *ca*. 25 to *ca*. 17%
550 passing from HAP/CMC4 to HAP/CMC16. MB pollution is instead fully remediated by all
551 composites containing a CMC content higher than *ca*. 4 wt.%, suggesting that a moderate CMC
552 content (i.e. *ca*. 8 wt.%) is adequate to impart to HAP/CMC composites proper adsorption properties
553 towards organic pollutants. Therefore, HAP/CMC8 emerged as the best performing composite, able
554 to assure the simultaneous removal of organic and inorganic polluting species.

555 *3.2.3 Adsorption kinetics on HAP/CMC8*

556 Adsorption kinetics of the three pollutants on HAP/CMC8 were investigated according to the
557 stirred batch adsorption methodology. Fig. a reports the concentration profiles of the pollutants as a
558 function of time (Table S4 and Table S5 report the numerical data).

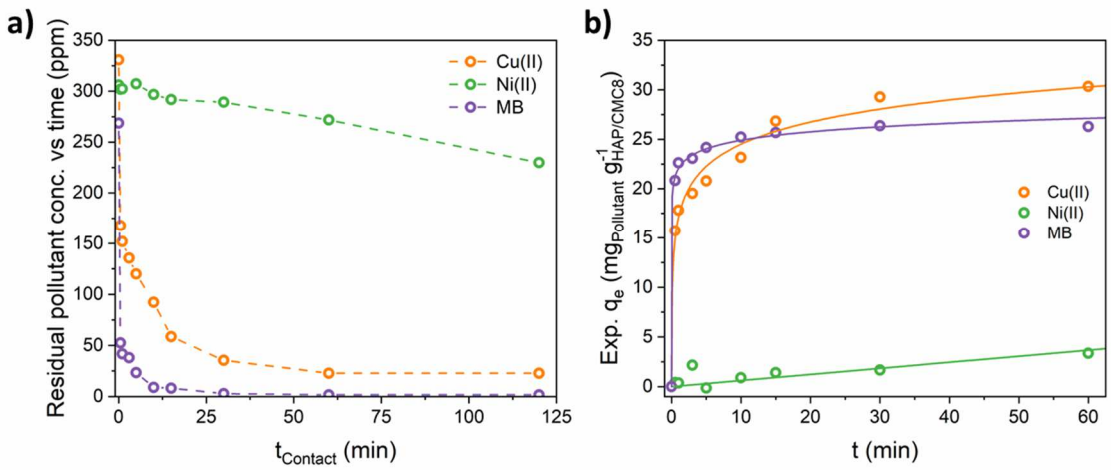

Fig. 8. a) Adsorption kinetics onto HAP/CMC8 composite in ternary solution: residual concentration of pollutants vs. time; b) fitting of experimental kinetic data with Elovich adsorption reaction model.

From a qualitative point of view, the curves reported in Fig. a disclose a defined trend in the adsorption rate of pollutants, being MB > Cu(II) > Ni(II). Kinetic curves of the MB and Cu(II) species exhibit an almost exponential decrease in their concentration within the first 10-15 minutes, reaching a stable value after *ca*. 30 and 60 minutes, respectively. On the opposite, Ni(II) adsorption kinetics was way more sluggish; a stable residual value could not be achieved within 2 h of test.

Experimental kinetic data were then non-linearly fitted according to three adsorption reaction models, which all find large application in describing the adsorption phenomena at the liquid-solid interface [26]: pseudo-first-order (PFO), pseudo-second-order (PSO) and Elovich models. Figure 8b reports the kinetic data fitted according to the Elovich model (the optimal kinetic parameters are collected in Table 4) which was the best model for our data (PFO and PSO fittings and experimental data are collected in Table S5).

Although Elovich adsorption reaction model is an empirical equation with no definite physical meaning [26], it could be meaningful in terms of comparison of the adsorption kinetics of different species on a sorbent. Initial adsorption rate (represented by the Elovich equation parameter *a*) of MB onto HAP/CMC8 approaches infinite, consistently with the concentration versus time curve reported

in Fig. a. Fast initial adsorption rate are calculated for Cu(II) as well, while on the opposite Ni(II) adsorption resulted *ca*. 4 order of magnitudes slower.

Table 4. Non-linearly regressed Elovich adsorption reaction model equation for pollutants adsorption onto HAP/CMC8 in ternary solutions.

Pollutant	***a***	***b***	R^2
	$mg \cdot g^{-1}\ min^{-1}$	$g \cdot mg^{-1}$	-
Cu(II)	636.8	0.310	0.987
Ni(II)	0.062	0.0045	0.912
MB	$\approx 7 \cdot 10^7$	0.808	0.997

3.2.4 Sorbent dosage effect

The effect of HAP/CMC8 dosage on the sorption performance were investigated by contacting the sorbent with the ternary mixture solution employing different solid to volume ratios. Residual pollutants concentrations after 2-hours long stirred batch adsorption tests at different HAP/CMC8 dosage are reported in Fig. , while numerical data are collected in Table S7.

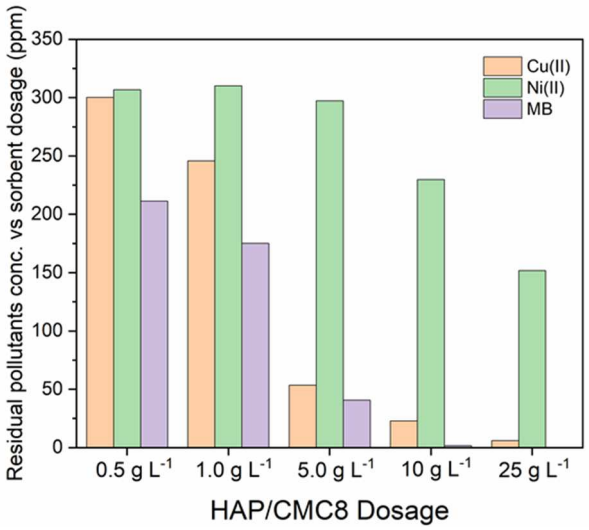

Fig. 9. Effect of HAP/CMC8 dosage on sorption performance of ternary mixtures: Cu(II)-Ni(II)-MB mixtures (initial concentrations of Cu(II) and Ni(II) of 300 ppm, each, and of MB of 250 ppm).

As expected, overall performances were enhanced by the increase in the sorbent dosage, although different trends were displayed by each pollutant. MB is progressively adsorbed for increasing solid to liquid ratio, with 10 $g_{HAP/CMC8}·L^{-1}$ representing the optimal sorbent dosage to completely remediate MB pollution. No competitive effect could be spotted between MB and metal cations, consistently indicating that MB trapping occurs preferentially on the carbonaceous moiety of the composite, towards which metal cations show limited affinity.

On the other hand, evidences of Cu(II) and Ni(II) competition (presumably on the hydroxyapatitic moiety of HAP/CMC8) may be detected. For sorbent dosage up to 5 $g_{HAP/CMC8}·L^{-1}$, Cu(II) adsorption seemed to take place preferentially to Ni(II) one. It is indeed evident that Ni(II) adsorption was increased when almost all Cu(II) have been removed from solution (at sorbent dosage 10 $g_{HAP/CMC8}·L^{-1}$) and that a major improvement in Ni(II) removal was achieved when sorbent dosage reaches the value of 25 $g_{HAP/CMC8}·L^{-1}$. Such a boost in the Ni(II) adsorption performance by HAP/CMC8 could be addressed to the disappearance of the competition with Cu(II) and the overall increase of sorbent active sites available for Ni(II) trapping.

3.2.5 Leaching tests

After being contacted with the solution containing the three pollutants (contact time 2 hours, sorbent dosage 10 $g_{HAP/CMC8}·L^{-1}$), selected samples, namely HAP and CMC pristine moieties and HAP/CMC8 composite, underwent leaching tests, as to assess the permanent nature of pollutants confinement onto their surfaces. The quantities of leached pollutants from the loaded sorbents are reported in Fig. .

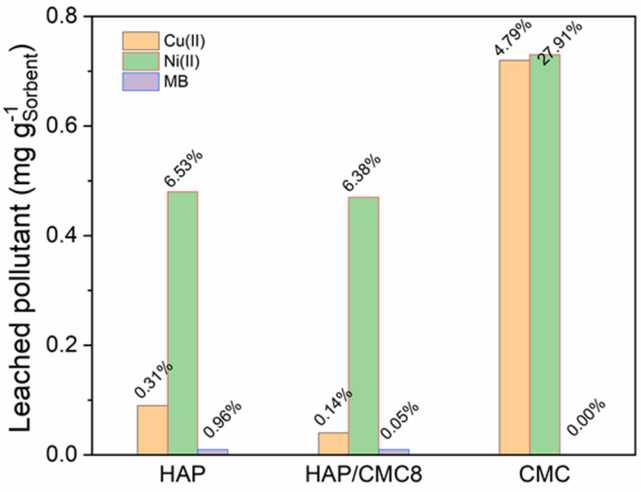

611

612 **Fig. 10.** Results of the leaching tests of pollutants from HAP, CMC, and HAP/CMC8 sorbents.

613

614 When contacted with fresh water, pollutants-loaded pristine HAP almost totally retained Cu(II)
615 and MB; it must however be considered that the latter is trapped in negligible amounts during the
616 prior adsorption test (Table 3). Conversely, a relevant leaching affects Ni(II), *ca*. 6.5% of the
617 immobilized Ni(II) was in fact released.

618 Pollutants-loaded pristine CMC shows whole retention of MB while major leaching phenomena
619 occurred for inorganic cations, despite the limited amount of Cu(II) and Ni(II) adsorbed during the
620 adsorption tests (Table 3).

621 Interestingly, HAP/CMC8 combines HAP and CMC permanent confinement features: Cu(II) and
622 Ni(II) leaching was indeed comparable to what observed for pristine HAP while an almost total
623 retention of MB was guaranteed by the CMC moiety of the composite.

624 *3.3 Preliminary economic considerations*

625 Adsorption is an easy and fast technology for wastewater treatment, whose processing costs are
626 essentially determined by production costs of adsorbents and energy consumption [37]. The price of
627 adsorbents is affected by several cost factors (e.g. labor costs, raw materials, energy consumption,
628 transport, taxes, storage). Although the adsorbent cost is a key factor for doing proper comparison,

629 just indicative estimates can be proposed, since the costs may vary enormously depending on the
630 availability of raw materials, countries, processing required.
631 The two components in the composite adsorbents, presented in this work, can be considered as low-
632 cost materials. Actually, taking into account costs deriving from chemicals (calcium nitrate,
633 diammonium phosphate, ammonium hydroxide solution), water and electricity [38], a production cost
634 of ca. 1.25 USD/kg can be estimated for synthetic hydroxyapatite. If the cost is seen in relation to the
635 adsorption capacity towards Cu(II), synthetic hydroxyapatite results on an equal footing with other
636 common low-cost sorbents (Table 5). If then hydroxyapatite was sourced from wastes, its use as
637 adsorbent would be even more convenient.
638 Similarly, concerning CMC, although literature data reported a production cost of around 3.24
639 USD/kg for analogous biomass activated carbon prepared using $ZnCl_2$ template [39], the high
640 adsorption capacity towards MB makes the CMC more convenient than other low-cost adsorbents
641 (e.g. fly ash, Table 5).
642 Finally, it is worth recalling another argument in favor, that is the possibility to achieve through
643 HAP/CMC composite materials the simultaneous remediation of inorganic and organic pollution,
644 with no negligible savings of time and money.
645

646 **Table 5.** Production costs and performance of some relevant low-cost sorbents

Material	Production costs (USD kg^{-1})	Target pollutant	Adsorption capacity ($mg \cdot g^{-1}$)	Ref.
Hydroxyapatite	1.25	Cu(II)	79.5	This work
Chitosan	16	Cu(II)	222	[40]
Bentonite	0.05	Cu(II)	4.75	[40]
Sphagnum peat moss	0.02	Cu(II)	14.3	[40]
CMC	3.24	MB	380	This work
Cement-carbon composite	5.99	MB	9.06	[41]
Coal fly ash	3.1	MB	28.65	[42]
n-Layer amino-functionalized graphene oxide	1900	MB	3036	[43]

647

3.4 Final remarks and conclusions

Hydroxyapatite is a multifunctional biomaterial which has high potentiality for successful application in the field of environmental management. A recent review highlighted the factors which make hydroxyapatite an eco-friendly material [11]. Actually, HAP is a biocompatible, no toxic compound, which can be sourced from several waste materials, thus contributing to mitigate environmental issues and costs associated with the disposal of these undesirable materials. Alternatively, hydroxyapatite can be synthesized starting from cheap precursors. A recent Life Cycle Assessment (LCA) study of nanohydroxyapatite preparation identified electricity consumption, H_3PO_4 production and transports for reagent acquisition as the three most environmentally damaging items with wide margins of improvement [44].

On the other hand, CMC is a porous carbon material prepared starting from soluble carbohydrate biomasses in the presence of the zinc chloride template. The use of cheap raw materials, the low impurity content of the resulting carbon materials as well as the easy removal and reuse of the template make the synthesis of CMC a facile and sustainable process [22].

Starting from HAP and CMC, eco-friendly HAP/CMC composites have been synthesized according to a simple co-precipitation route.

Extensive compositional, structural, morphological and surface characterization allowed rationalizing the effect of material composition on structural/morphological features and sorption performances. Thanks to the dual nature exhibited by the composites, simultaneous remediation of organic and inorganic pollution has been achieved in a one-step adsorption process, with the almost complete abatement of hazardous species concentrations. The obtained results demonstrate that a limited content of the carbonaceous moiety (*ca*. 8 wt.% CMC) is sufficient to impart optimal sorption performances.

Despite the appealing of eco-friendly and efficient materials, only a few publications report on the development of HAP/C composites as dual sorbents for simultaneous removal of organic and inorganic pollutants from wastewaters [20,45–48]. Besides, HAP/C sorption ability has been mainly

674 evaluated for inorganic benchmark pollutants (i.e. Pb(II) and Cu(II)), often individually present in
675 solution. Under these conditions, the carbonaceous moiety of the composites acts merely as
676 support/dispersant of the hydroxyapatitic one, without exerting any assessable sorption action.

677 In this scenario, the remarkable adsorption features and the permanent nature of pollutant
678 confinement onto the HAP/CMC composites presented in this study prove that simultaneous removal
679 of both organic and inorganic pollutants from wastewater may be achieved combining two eco-
680 friendly and easily available moieties like hydroxyapatite and activated carbons. This study may serve
681 as the starting point for the development of sustainable and multifunctional chemical formulations
682 for the environmental remediation. In the circular economy perspective, the next step should provide
683 for the formation of HAP/C composites directly from waste materials. In this regard, biogenic wastes,
684 with high content of both phosphate salts and carbohydrates, might represent the ideal raw materials
685 for the production of such composites.

686 Furthermore, additional studies will be aimed to assess the effect of naturally occurring
687 complexing agents (e.g. fulvic and humic acids) on the stability and adsorption capacity of
688 composites, as to evaluate their possible application in the remediation of real wastewaters.

689

690

691 ## 4. ACKNOWLEDGEMENTS

692

693 The authors kindly acknowledge: Pr Monica Dapiaggi, from Dipartimento di Scienze della Terra,
694 Università degli Studi di Milano, for XRPD analyses, Pr Silvia Bruni and PhD student Margherita
695 Longoni for registering Raman spectra, Dr Marco Schiavoni for transmittance FT-IR spectra, and
696 PhD student Laurent Delafontaine, from University of California Irvine, for the help in editing the
697 grammar and phrasing of the manuscript.

698

699 ## 5. FUNDING

700 Authors gratefully acknowledge the funding from INAIL (bando INAIL BRIC 2016 – ID13).

6. REFERENCES

[1] WHO, Drinking Water Parameter Cooperation Project: Support to the revision of Annex I Council Directive 98 / 83 / EC on the Quality of Water Intended for Human Consumption (Drinking Water Directive) Recommendations, (2017).

[2] G. Gollavelli, C.C. Chang, Y.C. Ling, Facile synthesis of smart magnetic graphene for safe drinking water: Heavy metal removal and disinfection control, ACS Sustain. Chem. Eng. 1 (2013) 462–472. https://doi.org/10.1021/sc300112z.

[3] T. Bora, J. Dutta, Applications of nanotechnology in wastewater treatment-A review, J. Nanosci. Nanotechnol. 14 (2014) 613–626. https://doi.org/10.1166/jnn.2014.8898.

[4] G.K. Sarma, S. Sen Gupta, K.G. Bhattacharyya, Nanomaterials as versatile adsorbents for heavy metal ions in water: a review, Environ. Sci. Pollut. Res. 26 (2019) 6245–6278. https://doi.org/10.1007/s11356-018-04093-y.

[5] S. Wong, N. Ngadi, I.M. Inuwa, O. Hassan, Recent advances in applications of activated carbon from biowaste for wastewater treatment: A short review, J. Clean. Prod. 175 (2018) 361–375. https://doi.org/10.1016/j.jclepro.2017.12.059.

[6] S. Kalita, M. Pathak, G. Devi, H.P. Sarma, K.G. Bhattacharyya, A. Sarma, A. Devi, Utilization of: Euryale ferox Salisbury seed shell for removal of basic fuchsin dye from water: Equilibrium and kinetics investigation, RSC Adv. 7 (2017) 27248–27259. https://doi.org/10.1039/c7ra03014b.

[7] J.P. Vareda, A.J.M. Valente, L. Durães, Assessment of heavy metal pollution from anthropogenic activities and remediation strategies: A review, J. Environ. Manage. 246 (2019) 101–118. https://doi.org/10.1016/j.jenvman.2019.05.126.

[8] G.N. Hlongwane, P.T. Sekoai, M. Meyyappan, K. Moothi, Simultaneous removal of pollutants from water using nanoparticles: A shift from single pollutant control to multiple

726 pollutant control, Sci. Total Environ. 656 (2019) 808–833.
727 https://doi.org/10.1016/j.scitotenv.2018.11.257.

728 [9] Y. Liu, Y. Huo, X. Wang, S. Yu, Y. Ai, Z. Chen, P. Zhang, L. Chen, G. Song, N.S. Alharbi,
729 S.O. Rabah, X. Wang, Impact of metal ions and organic ligands on uranium removal
730 properties by zeolitic imidazolate framework materials, J. Clean. Prod. 278 (2021) 123216.
731 https://doi.org/10.1016/j.jclepro.2020.123216.

732 [10] Y. Liu, H. Pang, X. Wang, S. Yu, Z. Chen, P. Zhang, L. Chen, G. Song, N. Saleh Alharbi, S.
733 Omar Rabah, X. Wang, Zeolitic imidazolate framework-based nanomaterials for the capture
734 of heavy metal ions and radionuclides: A review, Chem. Eng. J. 406 (2021) 127139.
735 https://doi.org/10.1016/j.cej.2020.127139.

736 [11] M. Ibrahim, M. Labaki, J.M. Giraudon, J.F. Lamonier, Hydroxyapatite, a multifunctional
737 material for air, water and soil pollution control: A review, J. Hazard. Mater. 383 (2020)
738 121139. https://doi.org/10.1016/j.jhazmat.2019.121139.

739 [12] A. Fihri, C. Len, R.S. Varma, A. Solhy, Hydroxyapatite: A review of syntheses, structure and
740 applications in heterogeneous catalysis, Coord. Chem. Rev. 347 (2017) 48–76.
741 https://doi.org/10.1016/j.ccr.2017.06.009.

742 [13] S. Recillas, V. Rodríguez-Lugo, M.L. Montero, S. Viquez-Cano, L. Hernandez, V.M.
743 Castaño, Studies on the precipitation behavior of calcium phosphate solutions, J. Ceram.
744 Process. Res. 13 (2012) 5–10.

745 [14] J. Reichert, J.G.P. Binner, An evaluation of hydroxyapatite-based filters for removal of heavy
746 metal ions from aqueous solutions, J. Mater. Sci. 31 (1996) 1231–1241.
747 https://doi.org/10.1007/BF00353102.

748 [15] I. Mobasherpour, E. Salahi, M. Pazouki, Comparative of the removal of Pb2+, Cd2+and
749 Ni2+by nano crystallite hydroxyapatite from aqueous solutions: Adsorption isotherm study,

Arab. J. Chem. 5 (2012) 439–446. https://doi.org/10.1016/j.arabjc.2010.12.022.

[16] I. Mobasherpour, E. Salahi, M. Pazouki, Removal of nickel (II) from aqueous solutions by using nano-crystalline calcium hydroxyapatite, J. Saudi Chem. Soc. 15 (2011) 105–112. https://doi.org/10.1016/j.jscs.2010.06.003.

[17] M. Ferri, S. Campisi, A. Gervasini, Nickel and cobalt adsorption on hydroxyapatite: a study for the de-metalation of electronic industrial wastewaters, Adsorption. 0 (2019) 0. https://doi.org/10.1007/s10450-019-00066-w.

[18] M. Ferri, S. Campisi, M. Scavini, C. Evangelisti, P. Carniti, A. Gervasini, In-depth study of the mechanism of heavy metal trapping on the surface of hydroxyapatite, Appl. Surf. Sci. 475 (2019) 397–409. https://doi.org/10.1016/j.apsusc.2018.12.264.

[19] S. Campisi, C. Evangelisti, G. Postole, A. Gervasini, Combination of interfacial reduction of hexavalent chromium and trivalent chromium immobilization on tin-functionalized hydroxyapatite materials, Appl. Surf. Sci. 539 (2021) 148227. https://doi.org/10.1016/j.apsusc.2020.148227.

[20] Y. Wang, L. Hu, G. Zhang, T. Yan, L. Yan, Q. Wei, B. Du, Removal of Pb(II) and methylene blue from aqueous solution by magnetic hydroxyapatite-immobilized oxidized multi-walled carbon nanotubes, J. Colloid Interface Sci. 494 (2017) 380–388. https://doi.org/10.1016/j.jcis.2017.01.105.

[21] Y. Dai, N. Zhang, C. Xing, Q. Cui, Q. Sun, The adsorption, regeneration and engineering applications of biochar for removal organic pollutants: A review, Chemosphere. 223 (2019) 12–27. https://doi.org/10.1016/j.chemosphere.2019.01.161.

[22] Y. Huang, S. Hu, S. Zuo, Z. Xu, C. Han, J. Shen, Mesoporous carbon materials prepared from carbohydrates with a metal chloride template, J. Mater. Chem. 19 (2009) 7759–7764. https://doi.org/10.1039/b911011a.

774 [23] M. Ferri, S. Campisi, P. Carniti, A. Gervasini, J. Shen, Tunable acidity in mesoporous
775 carbons for hydrolysis reactions, New J. Chem. 44 (2020) 5873–5883.
776 https://doi.org/10.1039/d0nj00750a.

777 [24] P. Carniti, A. Gervasini, S. Biella, Determination of catalyst surface acidity in liquids by a
778 pulse liquid chromatographic technique, Adsorpt. Sci. Technol. 23 (2005) 739–749.
779 https://doi.org/10.1260/026361705776316587.

780 [25] P. Carniti, A. Gervasini, Liquid-Solid Adsorption Properties: Measurement of the Effective
781 Surface Acidity of Solid Catalysts BT - Calorimetry and Thermal Methods in Catalysis, in:
782 A. Auroux (Ed.), Springer Berlin Heidelberg, Berlin, Heidelberg, 2013: pp. 543–551.
783 https://doi.org/10.1007/978-3-642-11954-5_17.

784 [26] J. Wang, X. Guo, Adsorption kinetic models: Physical meanings, applications, and solving
785 methods, J. Hazard. Mater. 390 (2020) 122156.
786 https://doi.org/10.1016/j.jhazmat.2020.122156.

787 [27] L. Silvester, J.F. Lamonier, R.N. Vannier, C. Lamonier, M. Capron, A.S. Mamede, F.
788 Pourpoint, A. Gervasini, F. Dumeignil, Structural, textural and acid-base properties of
789 carbonate-containing hydroxyapatites, J. Mater. Chem. A. 2 (2014) 11073–11090.
790 https://doi.org/10.1039/c4ta01628a.

791 [28] Z.Q. Li, C.J. Lu, Z.P. Xia, Y. Zhou, Z. Luo, X-ray diffraction patterns of graphite and
792 turbostratic carbon, Carbon N. Y. 45 (2007) 1686–1695.
793 https://doi.org/10.1016/j.carbon.2007.03.038.

794 [29] Tuinstra F, Koenig JL, Raman Spectrum of Graphite, J. Chem. Phys. 53 (1970) 1126–1130.
795 https://doi.org/10.1063/1.1674108.

796 [30] D. Yamini, G. Devanand Venkatasubbu, J. Kumar, V. Ramakrishnan, Raman scattering
797 studies on PEG functionalized hydroxyapatite nanoparticles, Spectrochim. Acta - Part A Mol.

798 Biomol. Spectrosc. 117 (2014) 299–303. https://doi.org/10.1016/j.saa.2013.07.064.

799 [31] S. Campisi, C. Castellano, A. Gervasini, Tailoring the structural and morphological
800 properties of hydroxyapatite materials to enhance the capture efficiency towards copper(II)
801 and lead(II) ions, New J. Chem. 42 (2018) 4520–4530. https://doi.org/10.1039/C8NJ00468D.

802 [32] C.H. Giles, T.H. MacEwan, S.N. Nakhwa, D. Smith, Studies in adsorption. Part XI. A system
803 of classification of solution adsorption isotherms, and its use in diagnosis of adsorption
804 mechanisms and in measurement of specific surface areas of solids, J. Chem. Soc. 846 (1960)
805 3973. https://doi.org/10.1039/jr9600003973.

806 [33] C.H. Giles, D. Smith, A. Huitson, A general treatment and classification of the solute
807 adsorption isotherm. I. Theoretical, J. Colloid Interface Sci. 47 (1974) 755–765.
808 https://doi.org/10.1016/0021-9797(74)90252-5.

809 [34] A. Corami, S. Mignardi, V. Ferrini, Copper and zinc decontamination from single- and
810 binary-metal solutions using hydroxyapatite, J. Hazard. Mater. 146 (2007) 164–170.
811 https://doi.org/10.1016/j.jhazmat.2006.12.003.

812 [35] M.O. Corapcioglu, C.P. Huang, The surface acidity and characterization of some commercial
813 activated carbons, Carbon N. Y. 25 (1987) 569–578. https://doi.org/10.1016/0008-
814 6223(87)90200-4.

815 [36] A. Dąbrowski, P. Podkościelny, Z. Hubicki, M. Barczak, Adsorption of phenolic compounds
816 by activated carbon - A critical review, Chemosphere. 58 (2005) 1049–1070.
817 https://doi.org/10.1016/j.chemosphere.2004.09.067.

818 [37] S. De Gisi, G. Lofrano, M. Grassi, M. Notarnicola, Characteristics and adsorption capacities
819 of low-cost sorbents for wastewater treatment : A review, Sustain. Mater. Technol. 9 (2016)
820 10–40. https://doi.org/10.1016/j.susmat.2016.06.002.

821 [38] Q. Shi, M. Su, G. Yuvaraja, J. Tang, L. Kong, Development of highly efficient bundle-like

hydroxyapatite towards abatement of aqueous U(VI) ions : Mechanism and economic assessment, J. Hazard. Mater. 394 (2020) 122550. https://doi.org/10.1016/j.jhazmat.2020.122550.

[39] Y.L. Jia, H.N. Lock, The production cost analysis of oil palm waste activated carbon : a pilot-scale evaluation, Greenh. Gases Sci. Technol. 28 (2020) 1–28. https://doi.org/10.1002/ghg.2020.

[40] V.K. Gupta, P.J.M. Carrott, M.M.L. Ribeiro Carrott, Suhas, Low-Cost Adsorbents: Growing Approach to Wastewater Treatment—a Review, Crit. Rev. Environ. Sci. Technol. 39 (2009) 783–842. https://doi.org/10.1080/10643380801977610.

[41] S. V Manjunath, R.S. Baghel, M. Kumar, Environmental Technology & Innovation Performance evaluation of cement – carbon composite for adsorptive removal of acidic and basic dyes from single and multi-component systems, Environ. Technol. Innov. 16 (2019) 100478. https://doi.org/10.1016/j.eti.2019.100478.

[42] N.T. Dinh, N. Hoang, T. Thanh, D. Phan, Enhancing the removal effi ciency of methylene blue in water by fly ash via a modified adsorbent, RSC Adv. 11 (2021) 20292–20302. https://doi.org/10.1039/d1ra02637b.

[43] T. José, M. Fraga, Z. Santana, B. De Souza, Comparative approach towards the adsorption of Reactive Black 5 and methylene blue by n - layer graphene oxide and its amino - functionalized derivative, Adsorption. 26 (2020) 283–301. https://doi.org/10.1007/s10450-019-00156-9.

[44] C. Ingrao, E. Vesce, R.S. Evola, E. Rebba, C. Arcidiacono, G. Martra, R. Beltramo, Chemistry behind leather : Life Cycle Assessment of nano- hydroxyapatite preparation on the lab-scale for fi reproo fi ng applications, J. Clean. Prod. 279 (2021) 123837. https://doi.org/10.1016/j.jclepro.2020.123837.

[45] Y. Long, J. Jiang, J. Hu, X. Hu, Q. Yang, S. Zhou, Removal of Pb(II) from aqueous solution by hydroxyapatite/carbon composite: Preparation and adsorption behavior, Colloids Surfaces A Physicochem. Eng. Asp. 577 (2019) 471–479. https://doi.org/10.1016/j.colsurfa.2019.06.011.

[46] Y. Zhu, Y. Jiang, Z. Zhu, H. Deng, H. Ding, Y. Li, L. Zhang, J. Lin, Preparation of a porous hydroxyapatite-carbon composite with the bio-template of sugarcane top stems and its use for the Pb(II) removal, J. Clean. Prod. 187 (2018) 650–661. https://doi.org/10.1016/j.jclepro.2018.03.275.

[47] Z. Ruan, Y. Tian, J. Ruan, G. Cui, K. Iqbal, A. Iqbal, H. Ye, Z. Yang, S. Yan, Synthesis of hydroxyapatite/multi-walled carbon nanotubes for the removal of fluoride ions from solution, Appl. Surf. Sci. 412 (2017) 578–590. https://doi.org/10.1016/j.apsusc.2017.03.215.

[48] K.W. Jung, S.Y. Lee, J.W. Choi, Y.J. Lee, A facile one-pot hydrothermal synthesis of hydroxyapatite/biochar nanocomposites: Adsorption behavior and mechanisms for the removal of copper(II) from aqueous media, Chem. Eng. J. 369 (2019) 529–541. https://doi.org/10.1016/j.cej.2019.03.102.

SUPPORTING MATERIAL

Tuning the sorption ability of hydroxyapatite/carbon composites for the simultaneous remediation of wastewaters containing organic-inorganic pollutants

Michele Ferri, Sebastiano Campisi, Laura Polito, Jiany Shen, Antonella Gervasini

S1 Experimental details

S1.1 Operative conditions in materials characterization

Herein the operative conditions applied in materials characterization are detailed.

Thermogravimetric analyses (TGA): In a typical TGA experiment, *ca*. 10 mg of HAP/CMC composite were weighted in a crucible and pyrolyzed according to the following thermal ramp:

- Heating from RT to 120°C at 10.00°C min^{-1} under flushing N_2 (flowrate 20.00 mL min^{-1});
- Isothermal step at 120°C under flushing N_2 (flowrate 20.00 mL min^{-1}) for 60 minutes;
- Heating from 120 to 800°C at 5.00°C min^{-1} under flushing air (flowrate 20.00 mL min^{-1});
- Cooling down to RT at 20°C min^{-1} under flushing N_2 (flowrate 20.00 mL min^{-1}).

N_2 ads/des isotherms: N_2 adsorption-desorption isotherms were collected at liquid nitrogen temperature, by means of a Sorptomatic 1990 version instrument from Thermo Scientific (Carlo Erba). The analysis was controlled by computer processing using MILES-200 program and MILEADP software for computations. Low-pressure part of the adsorption branch of the isotherm has been modeled according to the 3-parameter BET equation ($0.005 < p/p^0 < 0.4$) as to determine specific surface area (S_a). The desorption branch has been interpreted by B.J.H. (Barrett-Joyner-Halenda) model ($0.3 < p/p^0 < 0.95$), thus obtaining the pore size distribution (PSD). Prior to the analysis, dried samples (*ca*. 150 mg) were outgassed for 4 h at 150°C under a residual pressure of 0.1

885 mbar, in order to fully remove water from meso and micropores. Nitrogen used for the analyses was
886 99.9995% purity.

887 *XRPD measures*: X-ray powder diffraction analyses were performed using a Philips Powder X-
888 ray diffractometer equipped with a PW 1830 generator, mounting a graphite monochromator,
889 operating with Cu Kα (λ = 1.5418 Å) radiation. The X-ray tube worked at 40 kV×40 mA. Diffraction
890 patterns were collected from 10° to 60° in 2θ, with a scan rate of 0.6° min^{-1} and a step size of 0.05°.
891 Phase identification was performed by Match! Software, from Crystal Impact GbR.

892 *TEM imaging*: Grids for TEM imaging were prepared as follows: for each sample, *ca*. 7 mg of
893 dried material were weighted, dispersed and sonicated in water for 15 minutes. The suspension was
894 further homogenized in a vortex mixer (*ca*. 10 s) and then diluted (dilution factor 1:100). 10 μL of
895 the resulting suspension were dropped on dried 300 mesh formvar/carbon copper grids (Cu 300 FC).

896 *Transmission FT-IR*: Spectra were collected on pads made from mixtures of dried samples (16 h
897 at 120°C under air) and dried KBr (FT-IR grade, from Sigma-Aldrich), with a constant sample to KBr
898 weight ratio of *ca*. 1:30.

899 *Raman spectra*: Raman spectra have been collected on a micro-Raman spectrometer equipped
900 with a Jasco RPM-100 probe, provided with a notch filter and an Olympus 50x objective and
901 interfaced to the laser and to a Lot-Oriel MS125 spectrometer. Cooling of the detector (Andor CCD,
902 1024 × 128 pixels) was operated by a Peltier device. A frequency-doubled Nd:YAG laser emitting at
903 532 nm was used as excitation source. Spectra have been collected with an acquisition time of 4 s
904 (100 spectra accumulation, background corrected).

905 *Surface acidity/basicity determination*: Surface acid-basic features have been determined
906 according to a pulsed-injection method, operated on a modified HPLC line. Previous to the
907 experiment, *ca*. 20 mg of dried sample were crushed, sieved as 80-200 mesh particles, and placed in
908 a sample holder (stainless steel tube, Ø = 2 mm, h = 12 cm) between two sand pillows. The sample
909 was thermally treated to ensure the full removal of water from meso and micropores (3 h at 150°C
910 under flowing air at flowrate of *ca*. 7 mL min^{-1}). After vacuum-wetting with the solvent of choice,

911 the sample holder was placed on the modified HPLC line and thermostated at 30°C. A typical analysis
912 was performed under a liquid flow rate of 5 mL min^{-1}. Regular injections of known amounts of probe
913 solution were performed (Δt_{inj} = 5 min, 10 µL of *ca*. 0.12 M PEA in both solvents for acid sites
914 titration; Δt_{inj} = 40 min and 40 µL of *ca*. 0.05 M BA in cyclohexane and *ca*. 0.025 M in water for
915 basic sites titration), thus obtaining a chromatogram composed of successive and increasing peaks.
916 The differences in the Δt_{inj} and in the probe V_{inj} between acidity and basicity measures origins from
917 the different adsorption kinetics of PEA and BA, the latter being characterized by a slow and constant
918 desorption under high solvent flowrate, thus hampering a precise collection of experimental point at
919 small Δt_{inj} (see Fig. *S2* for two typical titration chromatograms). Saturation was considered to be
920 achieved (i.e. complete titration of all surface sites) when constant peak~~s'~~ height and area were
921 obtained for 3 consecutive injections. Mathematical interpretation of the results can be found in the
922 following paragraph.

923 *Evaluation of HAP/CMC composites sorption ability*: Adsorption tests were performed according
924 to a stirred batch setup described in the main text. Quantification of the initial and final Cu(II) and
925 Ni(II) concentrations have been carried out using a Dionex DX-120 chromatograph equipped with a
926 Dionex IonPacTM CS5A 4 x 250 mm column (eluent: 50 mM Oxalate/95 mM lithium hydroxide pH
927 4.80), a derivatization system (post-column reagent: 0.4 mM 4-(2-pryidylazo)resorcinol (PAR) / 1 M
928 acetic acid / 3 M ammonium hydroxide) and a Merck Hitachi L-4200 UV/Vis detector. Copper and
929 nickel standards (1,000 µg/mL, 2% HNO_3 from Perkin Elmer) were used for IC-UV Vis calibrations.
930 Initial and final MB concentration were instead determined by UV-visible spectrophotometry
931 (Shimadzu UV–3600 spectrophotometer) at fixed wavelength (λ_{max} = 662 nm).

932 *S1.2 Acid-base pulsed-injections titration method*

933 In a pulsed-injections titration, dosed amount of acid or basic probe molecules are sent to the
934 sample, collected in a sample holder as described in the "Materials and methods" Section, under a
935 continuous flow of the pure solvent of choice.

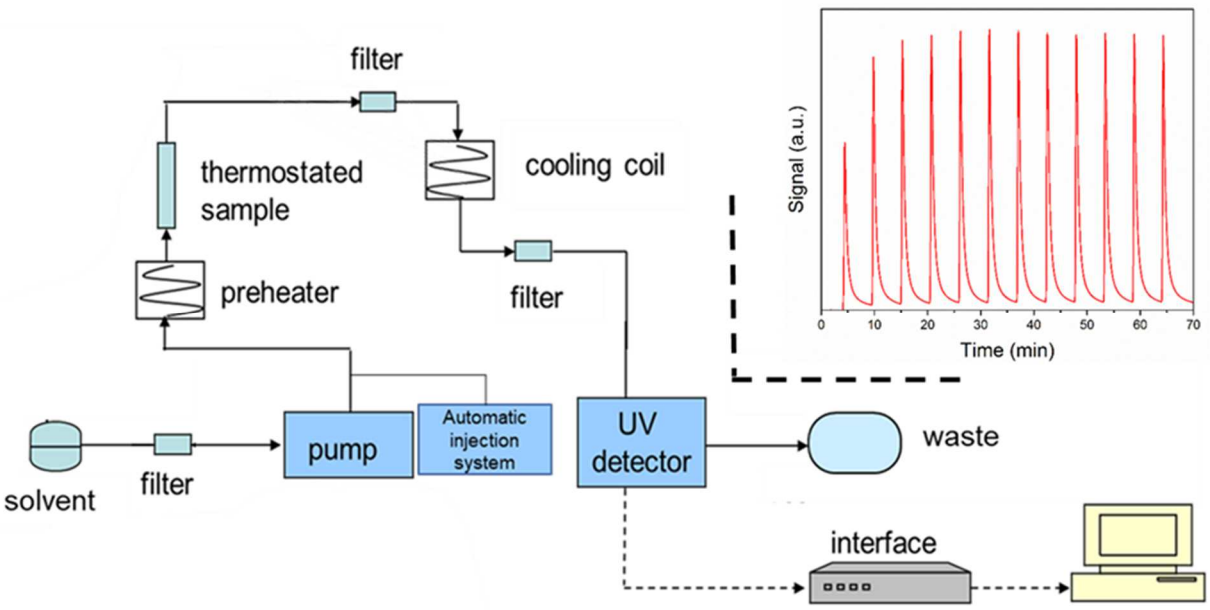

936

937 **Fig. S1.** Scheme of the modified HPLC line for pulsed-injection liquid-solid acid-base titrations (main
938 figure) and a typical chromatogram obtained from an acid/basic titration (inset).

939 In the configuration reported in Fig. *S1*, the non-adsorbed probe is revealed by the UV-vis
940 detector as a peak (inset in the upper right corner of Fig. *S1*). The integrated peak area can be directly
941 correlated to the quantity of probe itself after proper calibration. Thus, by difference with the (known)
942 amount of injected probe, it is possible to obtain the quantity of adsorbed probe molecules. As result
943 of the increasing surface saturation after each injection, the peaks area tends to increase accordingly,
944 as the quantity of probe adsorbed by the sample reduces. Once saturation is attained, the peaks display
945 a constant area, identifying the end point of the titration.

946 It is therefore possible to quantify the number of surface acid/base sites by computing the
947 amount of probe adsorbed and assuming a given stoichiometry (in this specific case, 1:1) between the
948 probe and the surface acid/base site:

949 $$\text{probe adsorbed}_i = \frac{[probe] \cdot V_{Inj}}{m_{cat}} \cdot \frac{A_{sat} - A_i}{A_{sat}}$$

950 where:

951 - probe adsorbed (mmol g^{-1}) = quantity of probe molecule adsorbed on the sample
952 during the i^{th} injection;

- [probe] (mol L^{-1}) = concentration of the injected probe (PEA or BA) solution;
- V_{Inj} (mL) = volume of the single i^{th} injection;
- m_{cat} (g) = mass of sample put in the sample holder;
- A_{sat} = average chromatographic area of the peaks at saturation (when constant area value is attained);
- A_i = chromatographic area of the i^{th} peak.

When a 1:1 stoichiometry between the probe and the site is assumed, the number of acidic/basic sites of the analyzed sample corresponds to the total amount of probe molecule adsorbed and it is possible to express the total number of surface acid/base sites of the sample as meq g^{-1} or meq m^{-2}.

In the following, two typical chromatograms, registered on HAP/CMC8 composite, when titrating with a) PEA and b) BA in cyclohexane under the operative conditions reported in the "Materials and methods" Section.

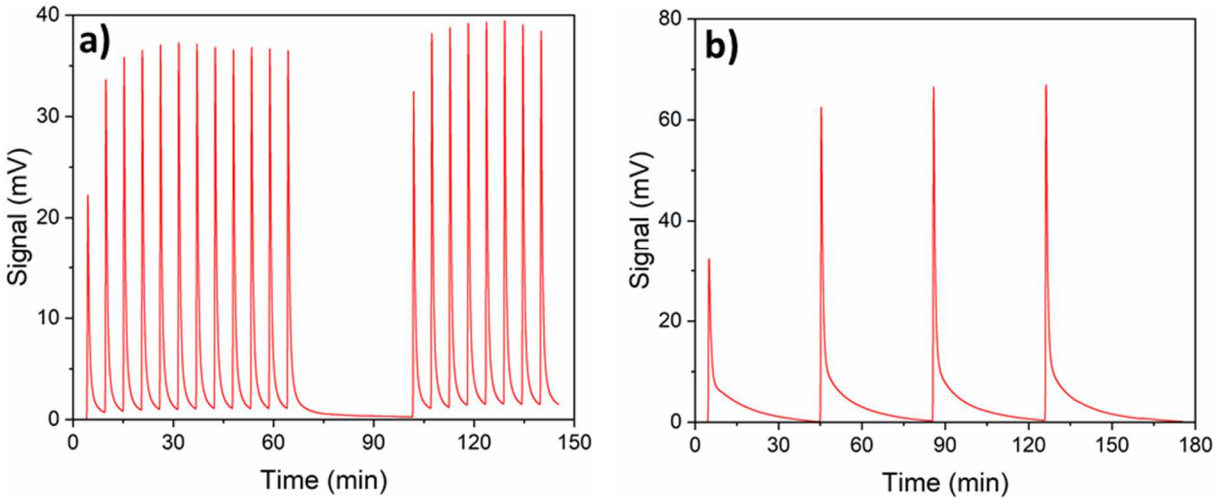

Fig. S2. Typical chromatograms registered on HAP/CMC composites under the operative conditions detailed in the "Materials and methods" Section. In the specific: a) acid sites titration with PEA in cyclohexane (i.e. intrinsic acidity); b) basic sites titration with BA in cyclohexane (i.e. intrinsic basicity).

S2 Characterization of HAP/CMC composites

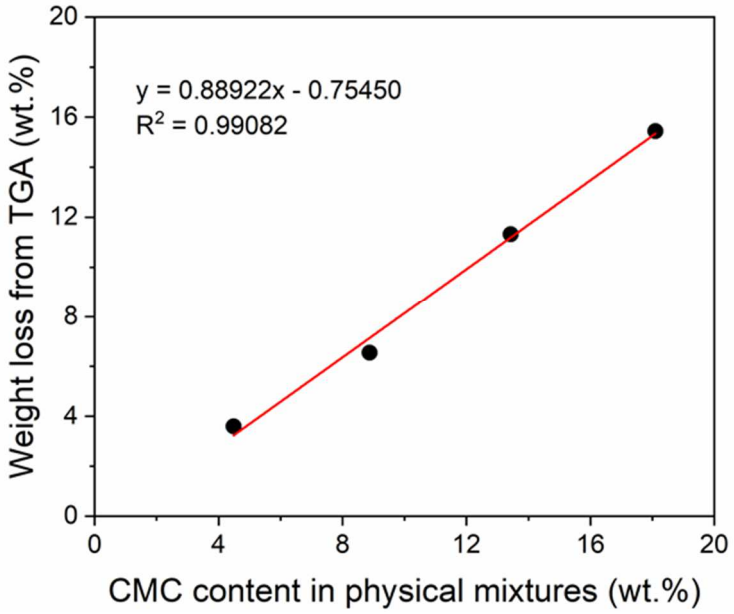

Fig. S3. Calibration line of thermogravimetric weight loss versus CMC content (wt.%) obtained from TG analyses on physical mixtures with known HAP:CMC massive ratio.

Table S1: Weighted masses of pristine HAP and CMC for the creation of HAP-CMC physical mixtures.

Sample - Physical mixture	m CMC	m HAP	CMC wt. %
	mg	*mg*	*%*
HAP-CMC4	4.9	104.3	4.49
HAP-CMC8	9.0	92.4	8.88
HAP-CMC12	13.9	89.6	13.43
HAP-CMC16	17.9	81.0	18.10

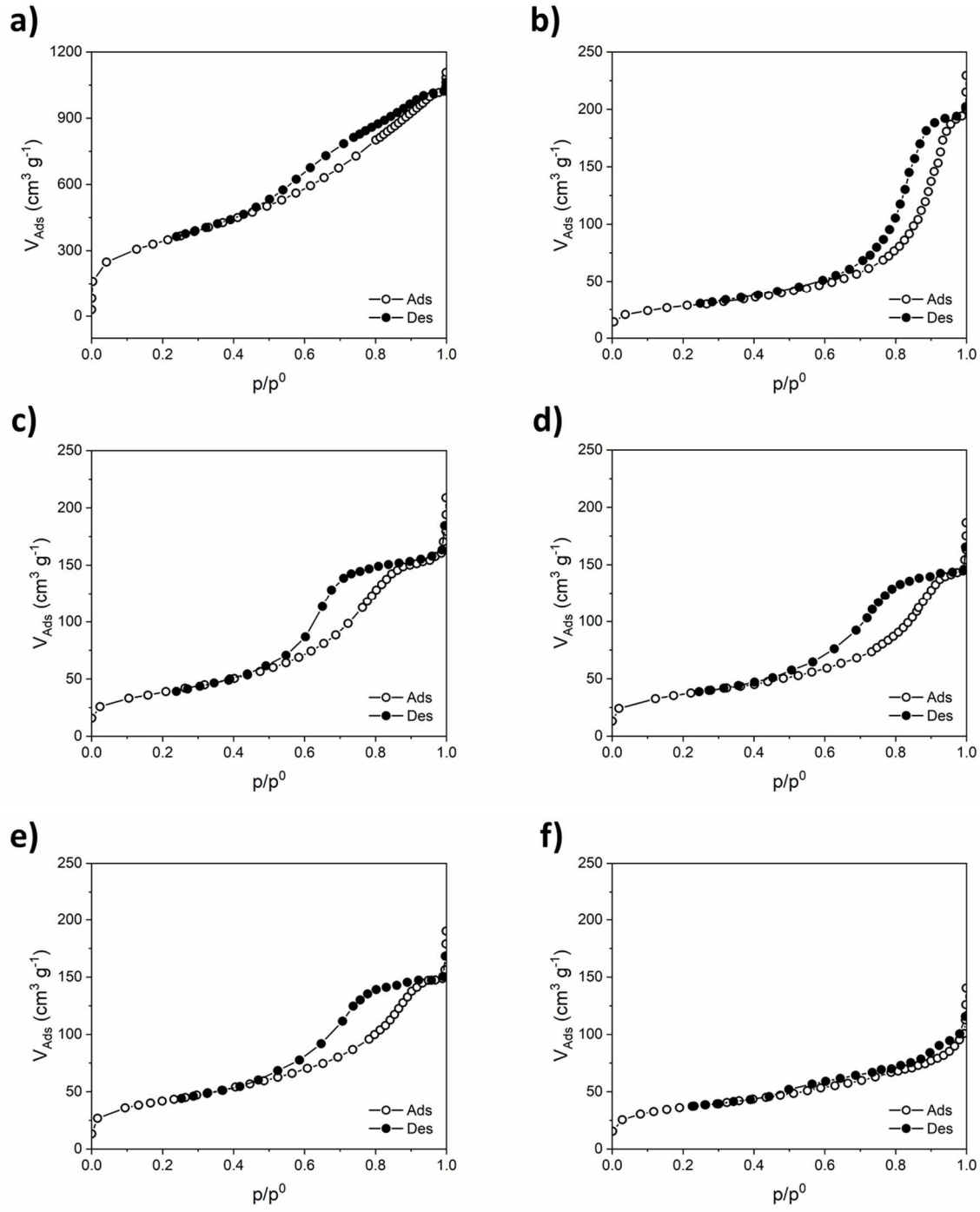

979

980 **Fig. S4.** N_2 adsorption/desorption isotherms registered on a) pristine CMC; b) pristine HAP; c)
981 HAP/CMC4; d) HAP/CMC8; e) HAP/CMC12 and f) HAP/CMC16.

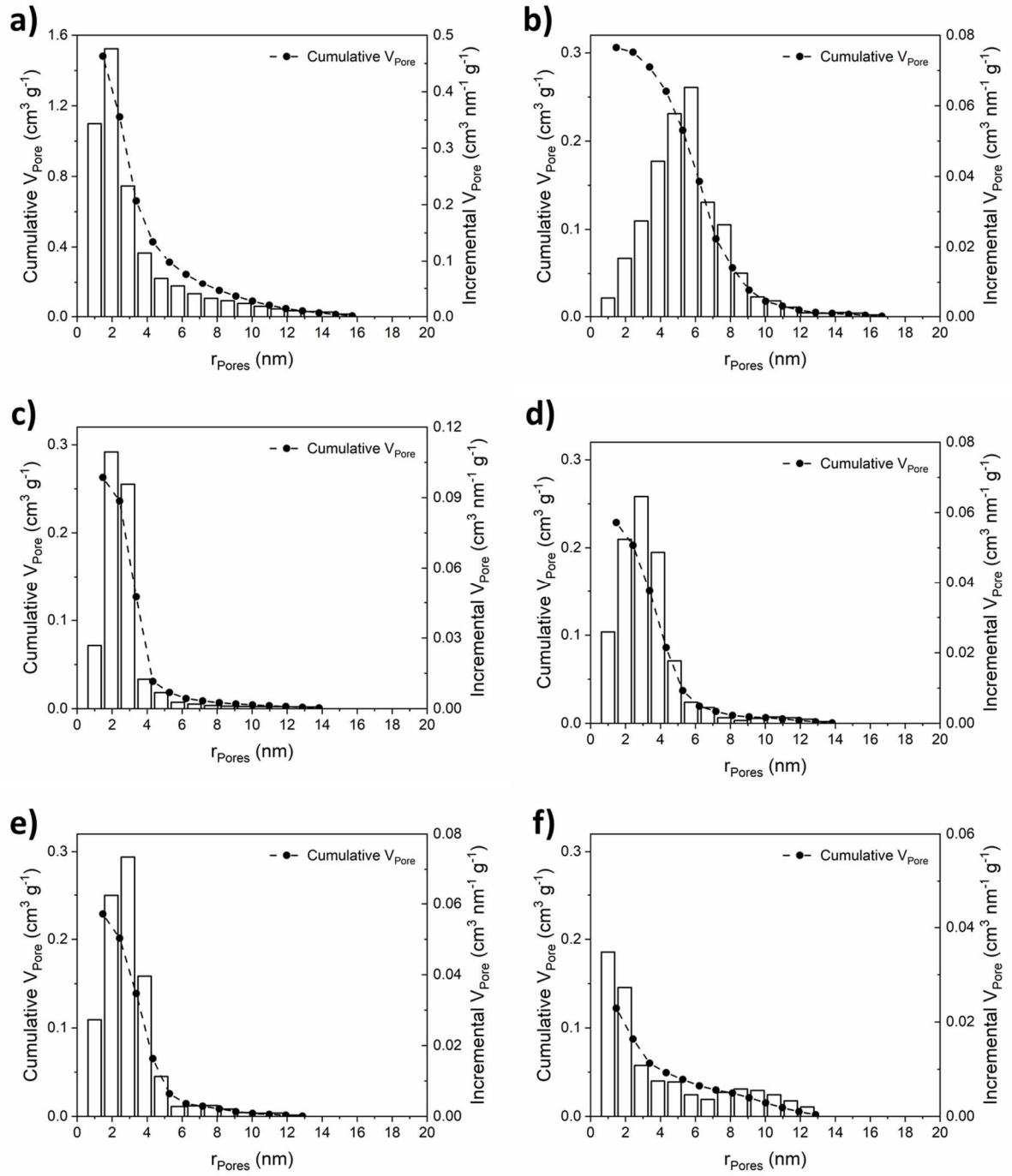

Fig. S5. Pore size distribution (PSD) calculated according to BJH method ($0.3 < p/p^0 < 0.95$) for a) pristine CMC; b) pristine HAP; c) HAP/CMC4; d) HAP/CMC8; e) HAP/CMC12 and f) HAP/CMC16.

989

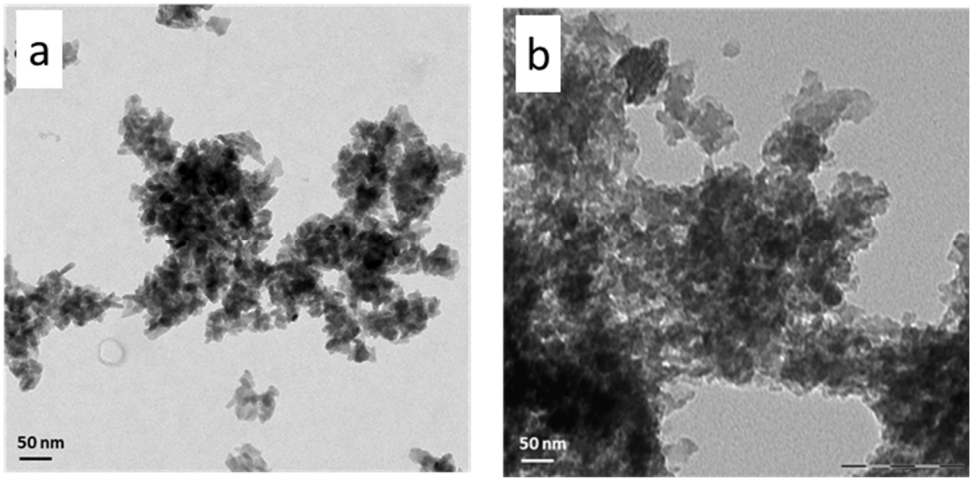

990

991 **Fig. S6.** TEM image of pristine HAP, a); and CM, b).

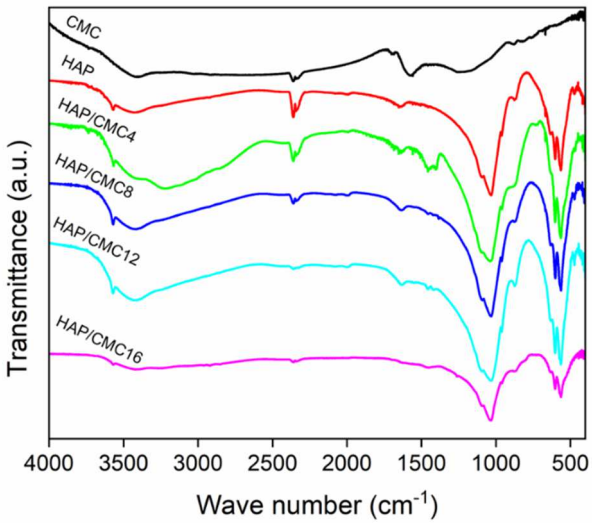

992

993 **Fig. S7.** FT-IR transmission spectra of pristine moieties and HAP/CMC composites.

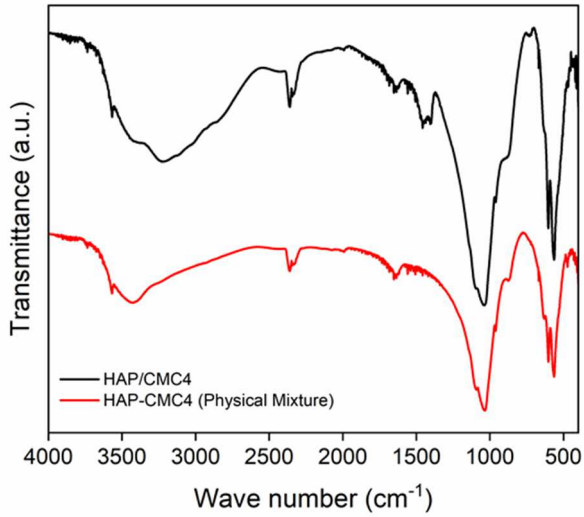

994

995 **Fig. S8**. Comparison between transmittance FT-IR spectra of HAP/CMC4 (composite) and HAP-
996 CMC4 (physical mixture).

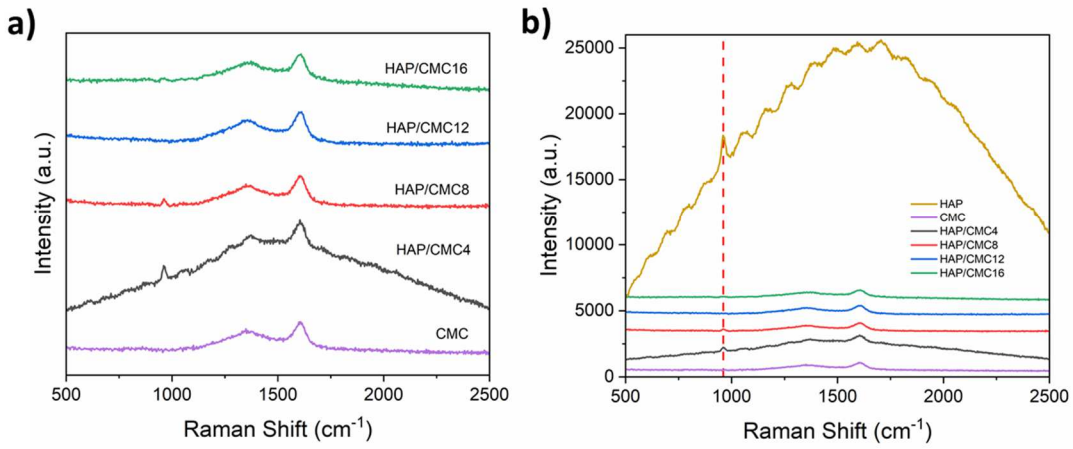

997

998 **Fig. S9**. Raman spectra collected on pristine moieties and HAP/CMC composites: a) pristine CMC
999 and HAP/CMC composite spectra and b) comparison of the high-intensity Raman spectrum of
1000 pristine HAP (yellow line) versus spectra collected on pristine CMC and HAP/CMC composites.

Table S2. Number/density of intrinsic (already presented in Table 1, reported here for the sake of clarity and comparison) and effective surface acid and basic sites of pristine moieties (HAP and CMC) and HAP/CMC composites.

Sample	Total acid sites				Total basic sites			
	Intrinsic (Cy)		Effective (H_2O)		Intrinsic (Cy)		Effective (H_2O)	
	meq g^{-1}	$\mu eq\ m^{-2}$	*meq* g^{-1}	$\mu eq\ m^{-2}$	*meq* g^{-1}	$\mu eq\ m^{-2}$	*meq* g^{-1}	$\mu eq\ m^{-2}$
HAP	0.221	2.197	N.D.	N.D.	0.016	0.156	N.D.	N.D.
HAP/CMC4	0.156	1.139	N.D.	N.D.	0.004	0.030	N.D.	N.D.
HAP/CMC8	0.089	0.687	N.D.	N.D.	0.006	0.048	N.D.	N.D.
HAP/CMC12	0.091	0.613	N.D.	N.D.	0.020	0.137	N.D.	N.D.
HAP/CMC16	0.021	0.174	N.D.	N.D.	0.003	0.024	N.D.	N.D.
Pristine CMC	0.251	0.203	0.355	0.240	0	0	N.D.	N.D.

S3 Sorption ability of HAP/CMC composites

Table S3. Complexation constants of the target metal species with the functional groups representing the main basic surface moieties of HAP.

Metal species	Log K_C [a]					
	-OH		-POH		-COOH	
	25°C	*μ = 0*	*25°C*	*μ = 0.5*	*25°C*	*μ = 0*
Cu(II)	6.3		3.2		9.6	
Ni(II)	4.1		2.1		6.9	

[a] K_C = Complex association constant, evaluated as [ML]/([M]·[L]), where ML is the metal-ligand complex, M the free metal cation and L the free anionic ligand.

[b] Measured at μ = 0

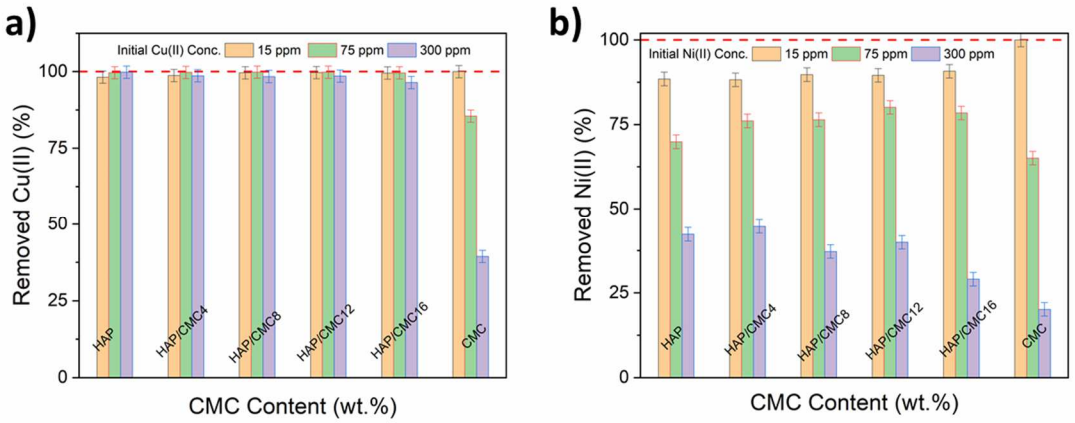

Fig. S10. Percentage removal of a) Cu(II) and b) Ni(II) achieved in single component solutions by pristine moieties and HAP/CMC composites, starting from different initial concentrations of pollutant species. Sorption tests performed according to a stirred batch method, T = 30°C, contact time = 2 h, pH 5.5 (± 0.5).

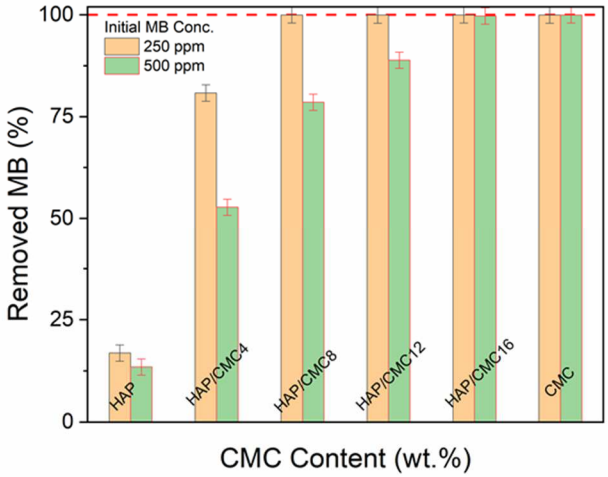

Fig. S6. Percentage removal of MB achieved in single component solutions by pristine moieties and HAP/CMC composites starting from different MB initial concentrations. Sorption tests performed according to a stirred batch method, T = 30°C, contact time = 2 h, pH 5.5 (± 0.5).

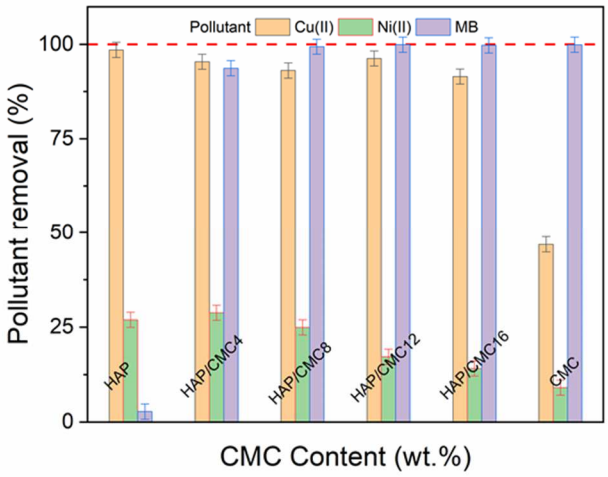

Fig. S7. Percentage removal of Cu(II), Ni(II) and MB achieved in ternary solutions by pristine moieties and HAP/CMC composites. Sorption tests performed according to a stirred batch method, T = 30°C, contact time = 2 h, pH 5.5 (± 0.5). Cu(II) and Ni(II) initial concentration was set at ca. 300 ppm while MB initial concentration was ca. 250 ppm.

Table S4. Kinetic data of pollutants adsorption onto HAP/CMC8 in ternary mixtures. On the left, residual concentration (ppm) vs. time; on the right, adsorbed amount of pollutants ($mg_{Pollutant}$ $g_{HAP/CMC8}^{-1}$) vs. time

Time *min*	**Residual pollutant concentration** *ppm*			**Adsorbed pollutant** $mg_{Pollutant}$ $g_{HAP/CMC8}^{-1}$		
	Cu(II)	*Ni(II)*	*MB*	*Cu(II)*	*Ni(II)*	*MB*
0	330.8	306.0	268.6	-	-	-
0.5	167.7	301.9	52.5	15.7	0.4	20.8
1	152.0	302.4	41.7	17.8	0.4	22.6
3	135.7	284.4	38.1	19.5	2.2	23.1
5	120.0	307.4	23.5	20.8	0.0	24.2
10	92.4	296.8	9.1	23.2	0.9	25.2
15	58.6	291.8	8.2	26.8	1.4	25.7
30	35.5	289.2	2.8	29.3	1.7	26.4
60	22.8	271.8	1.7	30.3	3.4	26.3
120	22.8	229.8	1.7	30.3	7.4	26.3

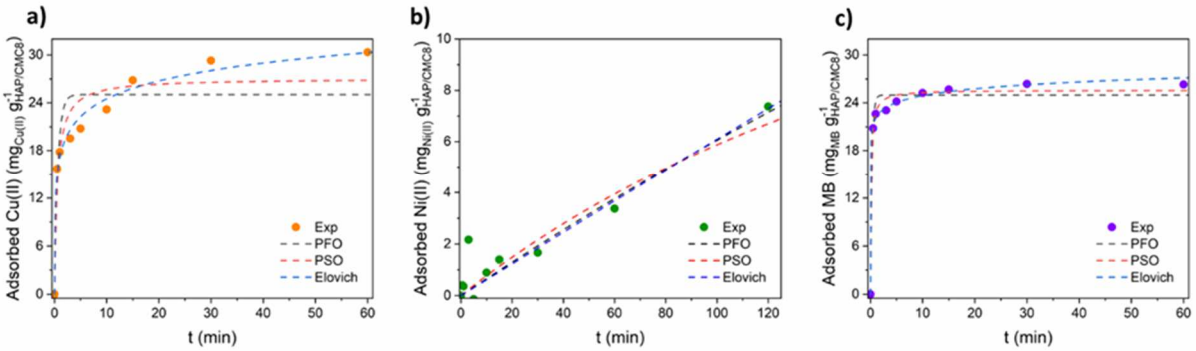

Fig. S8. a) Cu(II), b) Ni(II) and c) MB fitting of experimental kinetic data (full circles) with PFO (dotted black line), PSO (dotted red line) and Elovich (dotted blue line) adsorption reaction models.

Table S5. Non-linearly regressed parameters of pseudo-first-order (PFO), pseudo-second-order (PSO) and Elovich adsorption reaction models for pollutants adsorption kinetics onto HAP/CMC8 in ternary solutions.

Pollutant	PFO			PSO			Elovich		
	k_1	q_e	R^2	k_2	q_e	R^2	a	B	R^2
	min^{-1}	$mg\ g^{-1}$	-	$g\ mg^{-1}\ min^{-1}$	$mg\ g^{-1}$	-	$mg\ g^{-1}\ min^{-1}$	$g\ mg^{-1}$	-
Cu(II)	1.523	25.0	0.847	0.068	27.1	0.916	636.8	0.310	0.987
Ni(II)	0.0017	37.9	0.909	0.0002	22.4	0.892	0.062	0.0045	0.912
MB	3.338	25.0	0.980	0.303	25.6	0.992	67713150	0.808	0.997

Table S6. Calculated time-dependent adsorption rate (according to Elovich model) of pollutants onto HAP/CMC8.

t	Cu(II)	Ni(II)	MB
min	$mg_{Ads}\ g_{Sorbent}^{-1}\ min^{-1}$		
0	636.8	0.062	67713150
0.1	30.74	0.062	12.38
0.2	15.75	0.062	6.19
0.3	10.59	0.062	4.13
0.4	7.97	0.062	3.09
0.5	6.39	0.062	2.48
1	3.21	0.062	1.24
2	1.61	0.062	0.62
3	1.07	0.062	0.41
4	0.81	0.062	0.31
5	0.65	0.062	0.25
10	0.32	0.062	0.12
15	0.22	0.061	0.08
30	0.11	0.061	0.04
45	0.07	0.061	0.03
60	0.05	0.061	0.02
90	0.04	0.060	0.01
120	0.03	0.060	0.01

Table S7. Residual pollutant concentration (ppm) and amount of adsorbed pollutant ($mg_{Pollutant}$ L $g_{HAP/CMC8}^{-1}$) at different HAP/CMC8 dosage.

HAP/CMC8 dosage $g_{HAP/CMC8}\ L^{-1}$	**Residual pollutant concentration** *ppm*			**Adsorbed pollutant** $mg_{Pollutant}\ L\ g_{HAP/CMC8}^{-1}$		
	Cu(II)	*Ni(II)*	*MB*	*Cu(II)*	*Ni(II)*	*MB*
0.5	300.3	306.8	211.4	3.07	0.00	5.76
1	245.8	310.1	175.2	4.06	0.00	4.46
5	53.6	297.2	40.7	0.54	0.02	0.44
10	22.8	229.8	1.7	0.30	0.07	0.26
25	6.0	151.7	0.1	0.13	0.06	0.11

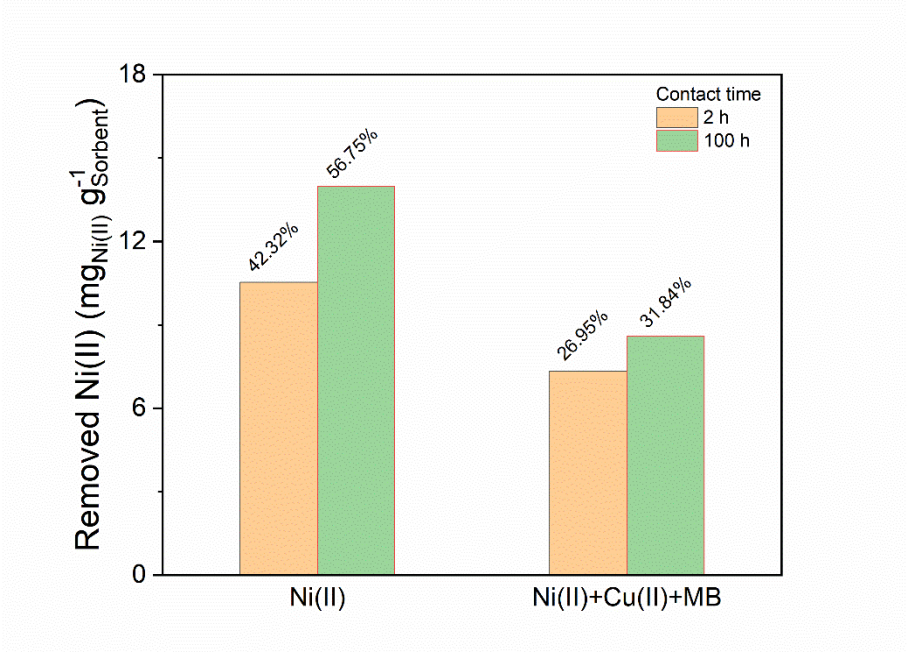

Fig. S9. Effect of contact time on the remediation efficiency of pristine HAP towards Ni(II) pollution. Initial Ni(II) concentration, both in individual (bars on the left) and ternary (bars on the right) solutions, is 300 ppm.